Bridging the muscle genome to phenome across multiple biological scales

SaiLavanyaa Sundar[1,3#*], Barbora Rimkus[1,3*], Prabath S. Meemaduma[2,3], Samuel deLap[1,3], Nicholas LaFave[1,3], Alice W. Racca[1,3], Pabodha Hettige[2,3], Jeffrey Moore[1,3], Matthew Gage[2,3], Andrea Shehaj[1,3], and Nicolai Konow[1,3#]

1. Department of Biological Sciences, University of Massachusetts, Lowell, UK
2. Department of Chemistry. University of Massachusetts, Lowell, UK
3. UMass Movement Center, University of Massachusetts, Lowell, UK

Correspondence to: SaiLavanyaa_Sundar@student.uml.edu and Nicolai_Konow@uml.edu
*These authors contributed equally to the research.

Key words: myosin isoforms, soleus, tibialis anterior, transcriptomics, shortening velocity, mouse

Summary Statement:

A multi-scale comparative study of muscles with different fiber type composition and architecture showing how intricate fine-tuning across gene, protein, and fascicle scales shape specialized muscle function.

ABSTRACT

Muscle is highly hierarchically organized, with functions shaped by genetically controlled expression of protein ensembles with different isoform profiles at the sarcomere scale. However, it remains unclear how isoform profiles shape whole muscle performance. We compared two mouse hind limb muscles, the slow, relatively parallel-fibered soleus (SOL) and the faster, more pennate-fibered tibialis anterior (TA), across scales: from gene regulation, isoform expression and translation speed, to force-length-velocity-power for intact muscles. Expression of myosin heavy-chain (MHC) isoforms directly corresponded with contraction velocity. The fast-twitch TA with fast MHC isoforms had faster unloaded velocities (actin sliding velocity, V_{ACTIN}; peak fiber velocity, V_{MAX}) than slow-twitch SOL. For SOL, V_{ACTIN} was biased towards V_{ACTIN} for purely slow MHC I, despite this muscle's even fast and slow MHC isoform

composition. Our multi-scale results clearly identified a consistent and significant dampening in fiber shortening velocities for both muscles, underscoring an indirect correlation between V_{ACTIN} and fiber V_{MAX} that may be influenced by differences in fiber architecture, along with internal loading due to both passive and active effects. These influences correlate with the increased peak force and power in the slightly more pennate TA, leading to a broader length range of near-optimal force production. Conversely, a greater force-velocity curvature in the near-parallel fibered SOL highlights the fine-tuning by molecular-scale influences including myosin heavy and light chain expression along with whole muscle characteristics. Our results demonstrate that the individual gene, protein, and whole fiber characteristics do not directly reflect overall muscle performance but that intricate fine-tuning across scales shapes specialized muscle function.

INTRODUCTION

Skeletal muscle is a tissue with highly hierarchical organization across multiple scales of biological organization. Muscle tissue also has an enigmatic capacity to meet highly diverse functional and physiological demands, ranging from slow, submaximal, and prolonged postural contractions to fast and powerful maximal contractions. At the finer organizational scales of molecules, genes, and proteins, the modulatory capacity of muscle is thought to correspond with the ensemble of motor proteins. The isoform makeup of these proteins can be highly heterogeneous and this heterogeneity shapes muscle contractile function at the coarser scales of sarcomeres, fibers, tissues, and the organ. At these coarser scales, muscle physiological function is also influenced by sarcomere architecture, and lengths during rest and operation. Hence, to define and relate the molecular- and protein-scale underpinnings of adaptations and reconcile them across muscles with different and specialized functions, an interdisciplinary multi-scale approach is needed. With few exceptions (Horak et al., 2016; Narici et al., 2016), such multi-scale analyses are lacking.

The precisely defined sarcomeric structure, combined with muscle's deeply hierarchical architecture influences the functional scope of muscle fibers such that the force production of skeletal muscle is highly length - and velocity - dependent (Lieber and Ward, 2011). Muscle contraction and force generation result from interactions between the thick (myosin-containing) and thin (actin-containing) filaments sliding past each other within sarcomeres (Huxley and Niedergerke, 1954; Huxley and Hanson, 1954). Thick and thin filament composition also influences muscle contractility. In particular, the myosin heavy chain (MHC) isoform composition within sarcomeres has been shown to define the speed of cross-bridge cycling, contractile efficiency, and also to influence the energy metabolism of different fiber types (Burke et al.,

1971; Hettige et al., 2020; Pette and Staron, 2000; Schiaffino and Reggiani, 2011; Wells, 1965). This isoform-dependency of converting chemical energy into mechanical energy by myosin has been used to establish a paradigm of characterizing muscle fibers as primarily fast-twitch (MHC IIa, MHC IIx, MHC IIb containing) and slow-twitch (MHC I containing) (Pellegrino et al., 2003). Varying populations of fast or slow twitch fibers can be identified in different muscles, from embryonic development to adult stages (Agbulut et al., 2003; Pette and Staron, 2000; Stål et al., 1994; Staron and Johnson, 1993) and thus the relative proportions of fast and slow muscle fibers provide an alternative avenue for muscles to vary contractile capabilities required to meet functional demands.

Several techniques have been used to study specific structural and functional attributes of muscle types, but such studies have mostly focused on single scales of biological organization rather than using a multi-scale approach. At the whole muscle scale, muscle ergometry studies have established differences in physiological properties between fast and slow twitch fibers (Close, 1964; Hill, 1938; Huxley, 1957) on the basis of force-length (FL), and force-velocity-power (FVP) relationships (Burkholder et al., 1994; Lieber and Fridén, 2000). At the protein scale, SDS-PAGE gel electrophoresis, immunohistochemistry, and *in-vitro* motility assays have been used to reveal the relative populations, ATPase rate and shortening velocities of slow- or fast-twitch fiber types (Höök et al., 1999; Pette and Staron, 2000; Schiaffino and Reggiani, 1994). Recent advances in RNA sequencing and other bioinformatics approaches have permitted exploration of the transcriptomic profile of muscles, allowing the identification of genetic and expression profiles of individual muscle types, but often lacking interrogation of functional relevance (Hettige et al., 2020; Terry et al., 2018). Therefore, multi-scale approaches that integrate knowledge about muscle contractile properties and protein isoform composition are necessary to link the gene, protein and whole muscle scales, to facilitate the integration of active and passive sarcomeric components, and to define the aggregate behavior of heterogeneous mixtures of myosins.

Here, we take an interdisciplinary approach to identify and characterize the key differences underlying the distinct functional properties of mouse soleus (SOL) and tibialis anterior (TA) at the genome, protein, and physiology scales. These muscles have distinct functional characteristics: mouse SOL is a fairly slow ankle plantar flexor (Asmussen and Maréchal, 1989; Holt and Askew, 2012) characterized by slow myosin isoform expression and relatively slow contraction velocities. Soleus also has a fairly parallel-fibered architecture (Burkholder et al., 1994) with reported pennation angles ranging from 5 to 11.4° (Brooks and Faulkner, 1988; Charles et al., 2016; Lal et al., 2021) and a slow-twitch, oxidative fiber composition (Asmussen and Maréchal, 1989; Burkholder et al., 1994), with a low energy cost (Westerblad et al., 2010). Mouse TA is a predominately fast-twitch ankle dorsiflexor (Burkholder and

Lieber, 1998) characterized by fast myosin isoform expression, relatively fast contraction velocities and a bipennate architecture (Burkholder et al., 1994; Charles et al., 2016; Moo et al., 2016), with reported pennation angles ranging from 11.7° to 24° and greater pennation angles being determined using non-destructive diffusion-tensor imaging (Burkholder et al., 1994; Charles et al., 2016; Heemskerk et al., 2005; Lovering et al., 2013). Correspondingly, TA muscles are composed of mainly fast-twitch, glycolytic fibers (Burkholder et al., 1994) with greater energy cost (Boss et al., 2018). A comparison of these structurally and functionally different muscles is useful for determining how differences in gene expression patterns (measured using Tag-Seq) influence protein expression, whilst not necessarily directly correlating to protein isoform distribution (measured via SDS-page) and unloaded translation speed for actin (measured via IVMA) and whole muscle (measured via ergometry).

We hypothesize that while myosin isoform expression strongly influences contraction force and speed (Pellegrino et al., 2003), contraction velocity is further refined at the muscle scale by additional, potentially contrasting and/or reinforcing, aspects of muscle fiber architecture (Bottinelli et al., 1991; Close, 1965; Lieber and Ward, 2011; Winters et al., 2011) that ultimately fine tune force- velocity curvature and the optimal force (F_{OPT}) and velocity (V_{OPT}) for peak power (Lutz et al., 2001). Due to the established correlation between specific myosin and titin isoform expression (Eckels et al., 2018; Freiburg et al., 2000; Linke et al., 1996; Prado et al., 2005; Trombitás et al., 1998), we will further test the hypothesis that active and passive muscle properties are tuned in combination to establish muscle functional phenotype. Our multi-scale approach indeed demonstrates that muscle shortening velocity is not a direct extrapolation from molecular actin sliding velocity, highlighting the importance of considering the influences in architectural, active, and passive muscle properties when assessing the causes of whole muscle function. Thus, contrary to general assumptions, overall muscle performance is imperfectly reflected by gene-, protein-, and fiber-scale characteristics, but instead shaped by intricate fine-tuning across-scales into the specialized function of individual muscles.

METHODS

All experiments were performed in accordance with approved IACUC protocols at both UML and Harvard University. Wildtype mice (body mass 32.1 ± 7.4 g; total n = 20; male n = 9, female n = 11) were obtained from an out-bred colony from no known specific strain and individually housed with *ad libitum* food and water access. Detailed procedures conducted at each organizational scale are described below.

Gene expression

RNA isolation, Tag-Seq library preparation and sequencing: Collected muscle samples were stored in RNAlater™ stabilization solution (ThermoFisher Scientific) at -80 °C until RNA extraction. Total RNA was extracted from five TA and SOL muscles (male n = 3 and female n= 2) using Qiagen fibrous tissue total RNA extraction mini kit. The concentration and quality of RNA were measured using the Qubit RNA Broad-Range assay and Agilent 2100 Bioanalyzer RNA 6000 Nano assay. 10 ng of total RNA from the extracted samples were used for Tag-Seq library preparation. The RNA integrity values (RIN) for these samples ranged from 5.4 to 7.8, with an average for all the samples being 7.06±0.96, which meets the recommended criteria in the Takara SMART-Seq Stranded protocol for Illumina sequencing platforms. The cDNA libraries were quantified using Qubit dsDNA HS kit (Thermo Fisher Scientific) and library sizes were quantified using an Agilent bioanalyzer 2100 High Sensitivity dsDNA assay. An extra quantification step was performed using qPCR with KAPA Library Quantification qPCR Kit for Illumina sequencing platforms. The cDNA libraries with concentration >3 ng/µl and average fragment size between 300–450 bp were sequenced with an Illumina NextSeq 500 sequencer using the sequencing guidelines suggested by Illumina.

Read preprocessing, alignment and counting: Quality of the short-read fragments generated from sequencing was assessed using the FastQC quality control tool for high throughput sequence data. Fastq files with a per base quality score below 20 were preprocessed using the sliding window quality filtering (window size 4) in Trimmomatic v0.32. Preprocessed short reads were aligned to Mus musculus GRCm38.p4 reference genome annotation using the alignment pipeline available on Github and archived in Eli-Meyers (Meyers July 2018 v2.0)

Differential expression analysis: Count files generated from the read alignments were obtained and used for downstream data analysis in R v3.6.1. Prior to the analysis, the genes with normalized read count less than 3 were removed to increase the sensitivity of differential gene expression. The differential gene expression analysis was performed between SOL and TA tissues using R library DESeq2. Significantly differentially expressed genes were identified at a 95% significance level using the Benjamini & Hochberg corrected p-values.

Variance stabilizing transformation was applied on the read counts to improve the homogeneity of variance and to normalize the counts, followed by removing batch effects and the noise in the dataset prior to data visualization.

Principal component analysis (PCA) was performed on selected differentially expressed genes. Differentially expressed genes were ranked based on the loading values of the first principal component and genes with highest contribution to the variance were selected using the cutoff (0.07) defined using the broken stick model (Jackson, 1993). Selected genes were visualized in an expression heatmap, the genes were grouped into four clusters (I-IV) based on their expression profiles (Figure 2C) using "Ward.D2" clustering method.

Percent Spliced-In index (PSI) calculation: PSI values for each exon coding for titin PEVK region were determined using the approach developed by (Schafer et al., 2015). *Mus musculus* GRCm38.100 genome annotation was used to extract titin exon coordinates and utilized as the reference exon annotation. Titin expression data for SOL (N=6) and TA (N=6) were gathered from the GEO database (accession number: GSE139204; 10 months old wildtype mice). Gathered RNA sequencing data were aligned to *Mus musculus* GRCm38.100 genome using the STAR alignment tool and used for the subsequent PSI calculations. Calculated PSI values range from 0-1; 1 being constitutive expression of the respective exon, while a value <1 indicates splicing events. A value 0 denotes complete exclusion of the exon from the expressed transcript pool.

Motor protein analyses

Protein purification: Myosin for *in-vitro* motility assay was extracted from chicken pectoralis (ch.sk.), mouse cardiac, TA and SOL muscles as previously described (Bárány, 1967; Malmqvist et al., 2004), but with modifications. Skeletal muscle tissue (~100-150 mg) was finely chopped and homogenized on ice after rinsing in 1X PBS buffer. Extraction buffer containing 300 mM KCl, 150 mM Imidazole, pH 6.8, 10 mM Na4P2O7, pH 6.8, 1 mM MgCl2, 2 mM DTT, and 1:100 ratio of protease inhibitor cocktail (MedChemExpress) was added to the muscle mince and stirred for 20 minutes at 4°C. After centrifugation at 200K*g* for 1.5 hours at 4°C, the supernatant was diluted 20-fold in 2 mM DTT. The protein precipitated overnight at 4°C and was then centrifuged at 30K *g* for 30 minutes at 4°C. The concentrated pellet was dissolved in 600 mM KCl, 2 mM MgCl2, 5 mM DTT, 10 mM Tris-HCl, pH 7.6. Myosin was stored in 50% glycerol at -20°C and myosin concentration was determined using spectrophotometer readings at 280 nm, corrected at 320 nm. Porcine cardiac actin was purified from acetone powder as previously described (Spudich and Watt, 1971).

SDS-PAGE: To determine myosin heavy chain isoform composition, purified chicken pectoralis, mouse cardiac, SOL, and TA samples from above were prepared for SDS- PAGE by diluting with 5X sample buffer (1.25 M Tris, pH 6.8, 48% (w/v) urea, 50% (w/v) sucrose, 5% (w/v) SDS, 0.5% (w/v)

bromophenol blue) to a final concentration of 0.13 mg/mL for chicken pectoralis, 0.16 mg/mL for cardiac, 1.13 mg/mL for SOL, 0.88 mg/mL for TA. Myosin isoforms in these samples were separated as previously described by (Blough et al., 1996), using a Mini- PROTEAN Tetra Cell (Bio- Rad Laboratories), with modifications. The stacking gel was 4% acrylamide:bis-acrylamide (with 30% glycerol) and the separating gel contained 8% acrylamide:bis-acrylamide (with 35% (v/v) glycerol). Both upper and lower gels were degassed prior to adding ammonium persulfate and TEMED, and the upper gel chamber was leak-proofed with a gel of ~ 1 % agarose in running buffer containing 0.025 M Tris, 0.192 M Glycine, 0.1% SDS. Gels were run for ~24-26 hours at 4°C, with additional 1% beta mercaptoethanol in the upper buffer chamber. Gels were stained with Coomassie blue dye and imaged using a Biorad ChemiDoc XRS Imaging System (Life Science, CA, USA). The densitometric analysis for determining the band intensities in the gel images were done using ImageJ as described previously (Sundar et al., 2020). These were averaged across three biological replicates (Figure 3) and tests of statistical significance between myosin isoform pairs in SOL and TA were performed on the GraphPad Prism 9 software, as an unpaired t-test where p-values less than 0.05 were considered significant.

In-vitro motility assay: Unregulated *in-vitro* motility assay was performed as per (Orzechowski et al., 2014) with modifications. Non-functional myosin was pelleted by diluting myosin with 1.1 μM actin and 1 mM ATP in myosin buffer containing 300 mM KCl, 25 mM Imidazole, 1mM EGTA, 4 mM $MgCl_2$, 10 mM DTT, pH 7.4. After centrifugation at 100,000 *g* for 30 minutes at 4°C, the myosin concentration in the supernatant was determined by Bradford assay (Bio-Rad Laboratories, Hercules, CA) and diluted to 100 μg/mL in myosin buffer. For slide preparation, a nitrocellulose coated cover-slip was placed on a standard glass slide with double-side tape, thereby forming a channel between the glass slide and the nitrocellulose surface. One volume (25 μL) of diluted myosin was loaded into the chamber and incubated for 1 minute, followed by a wash with 1 mg/mL bovine serum albumin (BSA) diluted in the myosin buffer to avoid any non-specific binding. Two volumes of actin buffer containing 55 mM KCl, 5 mM EGTA, 4 mM MgCl2, 10 mM DTT, pH 7.4 was flowed through the chamber before blocking any non-functional myosin with 1 μM actin diluted in actin buffer for 2 minutes. This was followed by two sequential washes of actin buffer containing 1 mM ATP, and then four washes with actin buffer, to remove any unbound actin. Actin labeled with TRITC was then added and allowed to interact with the myosin surface for 1 minute. One volume of motility buffer containing 10 mM calcium (pCa 4.0), 2 mM dextrose, 160 units of glucose oxidase, 2 μM catalase, and several concentrations of ATP (0 μM - 1 mM) was added to initiate motility of actin filaments.

***Data analysis and statistics*:** Data from 3 technical replicates were analyzed using the MTrackJ plugin in ImageJ (https://imagescience.org/meijering/software/mtrackj/). An average of 12-15 filaments were analyzed from each of the five movies recorded for each experiment to obtain the sliding velocity of actin under each condition. Data were then averaged to obtain mean actin sliding velocity with a standard deviation (S.D.) measurement and plotted in GraphPad Prism 8.0.2 where the Michaelis-Menten equation was fitted as $Y = (V_{MAX} * x) / (K_m + x)$ (1); where V_{MAX} is the maximal velocity of actin translation across myosin and K_M is the substrate concentration at half-maximal velocity. Statistical significance of V_{MAX} values between SOL and TA was determined by a two-tailed unpaired t-test with Welsh's correction and p-value < 0.05 was considered significant.

Ergometry on intact muscles

Surgical procedure: Muscle dissection and isolation was performed as previously detailed (Askew et al., 1997; Askew and Marsh, 1997; Hakim et al., 2013). Briefly, mice were deeply anesthetized by administering isoflurane via a nose cone (3% induction, 0.8% maintenance). Skin and surrounding connective tissues were carefully removed from one hindlimb. Room temperature (~23^0 C) Ringer's solution of pH 7.4 (composition in mmol/L: 144 NaCl, 6 KCl, 2 $CaCl_2$, 1 $MgSO_4$, 1 NaH_2PO_4, 10 glucose, 10 HEPES (Daut and Elzinga, 1989) was frequently applied to exposed tissue via syringe. The distal tendons of lateral and medial gastrocnemius were carefully dissected away from their attachment to the calcar and reflected. Similarly, the distal tendon of plantaris was cut and the muscle was carefully removed, to reveal soleus in the posterior compartment. The proximal and distal tendon of Soleus were then tied with braided 4/0 silk suture (Ethicon) at each myotendinous junction. Resting muscle length (L_{MUS}) was measured from knot to knot with the ankle held at 90° (Rassier et al., 1999). Both tendons were then cut and the muscle was immediately placed in a bath of circulated oxygenated Ringer's solution (pH 7.4 and 25°C, monitored via a thermometer). The suture at the distal end of Soleus was tied to a stopper and the proximal end to the lever arm of a 1N ergometer (Aurora Scientific Inc., model 300C-LR. Aurora, ON, CA) (Figure 1A). After mounting, the preparation was set to $L_{MUS.}$ *In-vitro* testing of SOL was commenced while the experimental limb was further dissected to isolate TA and secure a custom nerve-cuff around the sciatic nerve prior to mounting of TA (Figure 1B). The distal tendon of TA was tied to the lever arm of a 5N ergometer (Aurora Scientific Inc., model 305C. Aurora, ON, CA) using braided 3/0 silk suture (Ethicon). The patella tendon was secured to a metal rod on the stereotaxic stage that held the motor and the subject, to minimize in-series compliance of the preparation. The TA was covered with Ringers-soaked gauze and kept at a near-constant temperature of 25°C using an adjustable infrared lamp and a thermocouple. Both preparations were set to L_{MUS} and allowed to rest for 10 min following rigging.

Ergometry testing: To elicit contractions, electrical stimuli were transmitted via parallel platinum paddle electrodes (SOL) or a custom-made bipolar nerve cuff (TA), respectively, using a Grass stimulator (S48, Grass Technologies, West Warwick, RI, USA). Stimulation parameters were optimized by muscle to the following literature values; stimulation duration (SOL and TA: 300 ms), pulse width (SOL: 1.0 ms; TA: 0.2 ms), stimulation frequency (SOL and TA: 150 Hz) (Askew and Marsh, 1997; Hakim et al., 2013; Holt and Askew, 2012; James et al., 1995; Moran et al., 2005). For each experiment, stimulation was optimized to elicit supramaximal contractions (SOL and TA: 1-4V). A three-minute rest period was held between contractions. Changes of force, length, and stimulation voltage were recorded at 4 kHz via a NIDAQ A/D converter into IGOR pro (v. 8.0; Wavemetrics, Lake Oswego, OR, USA).

Force-length relationship: Force-Length (FL) curves (Figure 1E) were constructed for twitch and tetanic conditions to determine muscle optimal length (L_o). Starting from a length shorter than slack length (L_{slack}), muscles were subjected to isometric contractions at increasing lengths. Fit lines were constructed for active and passive force using third order polynomial fits in IGOR pro and maximum active force (P_o) and L_o were determined from these data fits. After normalizing active FL curves using tetanic L_o , we measured the tetanic and twitch plateau lengths. Tetanic L_o was used to determine starting length for remaining tests and P_o was used to monitor prep viability at regular intervals; experiments in which P_o decreased by more than 10% over the course of the experiment were excluded from further analysis. The width of the ascending limb of the active FL curve (henceforth called the plateau width) was measured as the range of strain from 90 - 100% P_o on the ascending FL curve limb. Slack length was measured for each preparation where passive force departed from zero. As an indication of relative differences in passive stiffness of the two muscles, we measured the force borne by the preparation at 110% L_o and the passive FL curve slope between L_o and 110% L_o.

Force-velocity-power relationship: Passive muscles were stretched to slightly above L_o and subjected to isotonic contractions against loads that were successively decreased between trials (Figure 1F). Velocity was calculated as the derivative of length and power was calculated as force × velocity. Using a custom implementation of the Hill equation $(P + a) \times (v + b) = b \times (P_o + a)$ in IGOR pro (Tijs et al., 2021), we then obtained Hill-fits for FV and PV data, and normalized FVP data to muscle mass specific force (N/g) and power (W/kg), optimal length (L_o/s) and maximum shortening velocity (%V_{MAX}). Optimal force (F_{OPT}) and velocity (V_{OPT}) were measured as the force and velocity respectively at which peak power was generated by the preparation. Force-velocity curvature was measured as a/P_o (Wilkie, 1949). After testing, muscles were carefully excised, free tendon was removed, and the belly was systematically blotted on Kim-wipes to remove moisture and weighed to the nearest 0.001g.

Statistical analysis of Force-Length and Force-Velocity-Power: General linear model (GLM) designs (Systat 11) were designed to test for statistical differences between muscles (mean ± S.D.) in each of the following variables: P_o, L_o, plateau-shift, plateau-width, slack length, passive stiffness, peak power, V_{max}, F_{opt}, and V_{opt}. For all tests, significance level (α) was set at 0.01. We disaggregated sex and individual in our GLM design and simplified the model when these factors were not statistically significant. Pooled samples were then analytically re-assessed between muscle groups.

RESULTS

Distinct transcriptomic profiles in SOL and TA

We studied gene expression profiles from Tag-Seq to determine differences in transcriptomic signatures between SOL and TA. Analyses of differential gene expression revealed 1061 genes with significant differences in expression between SOL and TA samples. PCA revealed a separation of slow and fast-twitch tissue along PC1, accounting for 73% of the variation in the dataset. Meanwhile, there was no differentiation of muscles along PC2 (Figure 2A). Given the lack of distinct sex-specific patterns, sex was not considered in subsequent gene analyses (Figure 2A). Loading values along PC1 were used to rank genes and identify the strongest transcriptomic features that distinguished SOL and TA. The "broken stick" approach (Jackson, 1993) revealed twenty-eight genes (descriptions provided in Supplementary Table 1) above the cutoff value of 0.07 for the gene loading values of PC1 (Figure 2B). An expression heatmap of genes above the selected cutoff showed four distinct gene-clusters, which were designated as gene clusters I-IV (Figure 2C). Since distinct expression pattern differences were observed within the clusters, and between the muscle types (Figure 2C), each cluster was analyzed to determine potential gene ontologies that correlated with the associated genes.

Genes that code for myosin heavy chain isoforms IIb (Myh4) and I (Myh7), which are typically expressed in fast-twitch and slow-twitch muscles respectively, were identified in clusters II and III. These two MHC isoforms also had distinct relative patterns of regulation in SOL and TA (Figure 2C). Gene ontologies classifying genes in each of the other clusters are provided in Supplementary Table 2. Cluster II has a common gene ontology in relation to muscle contraction, assembly and organization with significant transcriptomic differences observed for SOL and TA in myosin binding protein C2 (Mybpc2) and myosin heavy chain 4 (Myh4) genes. In cluster III, Myl3, Myh7, Tnnc1 and Tpm3 describe the protein ensemble making up the muscle sarcomeres. The genes in the clusters I and IV do not share any common gene ontologies.

Distinct myosin isoform expression in SOL and TA

Due to the distinct regulatory differences of Myh4 and Myh7 genes in SOL and TA, the expression levels of the genes coding for MHC isoform expression, specifically Myh1, Myh2, Myh4, Myh7, were compared as a measure of fragments per kilobase of transcript per million mapped reads (FPKM) (Figure 3A). Gene expression profiles of SOL muscle showed high levels of expression of the Myh7 gene and relatively lower levels of the faster myosin isoforms. High levels of Myh4 and Myh1 were identified in TA, with low expression of Myh2 and Myh7 genes. Myh1 and Myh2 are expressed at lower levels in both muscle types compared to Myh4 and Myh7.

To specifically identify differences in MHC isoform distributions at the protein scale, SDS-PAGE was used. Our results revealed clear differences in myosin isoform distributions where TA exhibited only fast isoforms while SOL contained a mixture of fast and slow isoforms (Figure 3C). Based on densitometric analysis of the gel bands and western blotting (not shown), the specific myosin isoforms were found to be statistically significant with average distributions of slow I (*Myh7*; 51%; $p < 0.05$) and fast IIa (*Myh2*; 49%; $p < 0.05$) in SOL, and predominantly fast IIb (*Myh4*; 69%; $p < 0.05$) and fast IIx (*Myh1*; 31%) in TA (Figure 3B). Despite low levels of Myh2 gene expression in SOL, the protein expression of fast IIa myosin was much higher, indicating translational-level amplification of Myh2 protein production.

Myosin isoforms shape *in-vitro* sliding velocities

Mean shortening velocities for myosin isolated from SOL and TA, across increasing ATP concentrations, were measured using an *in-vitro* motility assay (Figure 4A). Consistent with myosin expression profiles (Figure 2 & 3), myosin from SOL had a significantly lower velocity across all ATP concentrations when compared to myosin from TA, with a 3.3-fold decrease in velocity at a saturating ATP concentration of 1 mM ($t = 13.64$; $df = 3.645$; $p < 0.005$) (Figure 4B). Michaelis-Menten constants (Km), which defines the ATP concentration required for half-maximal activation, were calculated to be 42 ± 1.7 μM and 6.4 ± 1.9 μM for TA and SOL myosin, respectively. This result is consistent with differences in the protein expression profile (Figure 3), with TA consisting of only fast MHC isoforms whereas SOL consists of an almost even mix of fast and slow MHC isoforms.

Active and passive properties of whole-muscle performance

Muscle ergometry studies on SOL and TA samples were used to account for tissue-scale factors that determine whole muscle performance, and to delineate contributions of factors shaping active versus passive muscle functional attributes. Data from male and female samples were pooled for analyses (Figure 5 & 6) since GLM revealed no significant sex-differences for all response variables. Significant

differences between SOL and TA were, however, observed in the active (Figure 5A) and passive (Figure 6A) force-length, and force-velocity-power (Figure 7A) relationships.

Muscle mass-specific active tetanic force, measured at optimal length (L_o) was approximately 1.3-fold lower for SOL (18.0 ± 4.4 N/g) than for TA (23.4 ± 2.4 N/g) (Figure 5A, D), a difference that was statistically significant (ANOVA; $F_{1,21} = 15.3$; $p < 0.001$). The FL plateau width, measured at 90%P_o on the ascending limb for SOL (21.8 ± 3.1%L_o) and TA (20 ± 2.7% L_o) was not statistically significantly different ($F_{1,21} = 2.15$; $p = 0.16$) under tetanic activation (Figure 5B, C, F). When compared to the twitch plateau width for SOL (12.3 ± 2.0%L_o) and TA (15.5 ± 1.9%L_o), the tetanic plateau width was statistically significantly greater (SOL; $F_{1,14} = 25.49$; $p < 0.0001$. TA; $F_{1,12} = 9.14$; $p < 0.01$) and the left-shift of L_o with increased activation (twitch to tetanic) was 8.2 ±0.2% for both muscles and statistically significant ($F_{1,21} = 17.2$; $p < 0.001$).

Passive force-length relationships are shown in Figure 6A. We found passive force borne at 110% L_o to be statistically significantly different ($F_{1,19} = 61.86$; $p < 0.0001$), and lower for SOL (0.012 ± 0.005 N/g) than for TA (0.091 ± 0.035) (Figure 6B). There was no statistically significant difference in the slack length ($F_{1,20} = 0.41$; $p < 0.53$) of SOL (-15 ± 6.3%L_o) and TA (-16.7 ± 5.6%L_o) (Figure 6C). However, the passive FL curve slope was statistically significantly different ($F_{1,20} = 56.3$; $p < 0.0001$), suggesting that passive SOL ($\beta = 0.05 \pm 0.029$) is less stiff than TA ($\beta = 0.8 \pm 0.36$) across a physiologically relevant range of operating lengths (±10% L_o) (Figure 6D). Because titin is the primary filament responsible for passive stiffness in the muscle sarcomere, we calculated the Percent Spliced-in Index (PSI) for SOL and TA titin genes using RNA-Seq analysis of data retrieved from the GEO database (GSE139204) to determine differences in passive muscle force-length properties were related to titin expression differences. Alternative splicing-induced differences in the predicted size of expressed titin isoforms between the muscles revealed four regions of higher exon inclusion for SOL compared to TA (Figure 6E), consistent with previous findings that demonstrate that slower muscles typically express longer titin isoforms (Prado et al., 2005).

The relationship between muscle mass-specific force and fiber length-specific shortening velocity provides key information about muscle performance. The FV relationship revealed a significantly ($F_{1,18} = 59.5$; $p < 0.001$) lower peak shortening velocity (V_{MAX}) for SOL (4.6 ± 0.5 L_o/s) compared to TA (6.7 ± 0.4 L_o/s) (Figure 7A). The curvature of the FV relationship, as defined by the Hill-constant (a/P_o), was statistically significantly ($F_{1,17} = X22.3$; $p < 0.001$) greater for SOL (0.30 ± 0.09) than TA (0.49 ± 0.06) (Figure 7A). Finally, peak muscle mass-specific power was statistically significantly ($F_{1,23} = 91.3$; $p <$

0.001) lower for SOL (60.0 ± 25.6 W/kg) than TA (202.2 ± 48.3 W/kg), and optimal velocity (V_{OPT}) and force (F_{OPT}); the velocity and force where peak power is produced, respectively, were also statistically significantly (V_{OPT}: $F_{1,23} = 39.2$; $p < 0.001$; F_{OPT}: $F_{1,23} = 31.8$; $p < 0.001$) lower for SOL (1.1 ± 0.3 L_o/s.; and 5.6 ± 1.6 N/g) than for TA (1.9 ± 0.4 L_o/s; and 8.9 ± 1.2 N/g), as shown by the left-shifted power-velocity peak for SOL, when compared to TA (Figure 7B).

DISCUSSION

We took a multi-scale interdisciplinary approach to parse out the fundamental underpinnings of the protein ensemble involved in force and power generation across skeletal muscle lengths and speeds, specifically with respect to the thick filament motor protein, myosin, which has a well-recognized and major role in determining muscle contractile performance. We studied mouse SOL and TA muscles, which are distinct in their fiber type composition, architecture, energy metabolism, size, and physiological function, to determine these muscles' differences in MHC and titin isoform expression and distribution, *in vitro* translation of actin, and whole muscle force-length-velocity-power properties. Our results highlight that myosin isoform-dependent differences in sliding velocity of actin (V_{ACTIN}) at the molecular scale does not completely account for differences in whole muscle shortening velocities (V_{MAX}) between TA and SOL. In addition, our multi-scale approach has provided a deeper understanding of the fine-tuning of transcriptional, translational, active, and passive influences on whole muscle force generation and power output between different muscles, culminating towards specialized muscle function.

Our determination of the differences in gene expression profiles between the slow-twitch SOL and fast-twitch TA highlight the rich diversity that defines muscle fiber characteristics. PCA on SOL and TA transcriptomes revealed genes encoding for myosin isoforms as the key determinant differentiating two muscle types (Figure 2). Clusters II and III, identified through "Ward.D2" cluster analysis, specifically showed opposite expression patterns between SOL and TA, highlighting their significant transcriptomic-based influence on each muscle type. On the one hand, over-expression of fast-type isoforms Mybpc2 and Myh4 in Cluster II highlights the influence of these genes in defining the fast-twitch phenotype of TA, compared to the under-expression in SOL. Significant variability in Cluster III genes include opposite expression patterns in Myl3, Myh7, Tnnc1 and Tpm3 among two muscle types (Figure 2C). The genes Myl3 and Myh7 are typically associated with shortening velocity in slow cardiac tissue (Sitbon et al., 2021) and have high expression levels in SOL, as compared to TA. In addition, high levels of slow-muscle associated Tnnc1 and Tpm3 genes in Cluster III, and Tnni1, Tnnt1 in Cluster IV for SOL, also highlight the precise fine-tuning of isoform expression involved in altering muscle physiology. This is

because Tpm3, Tnnc1, Tnni1, Tnnt1 are critical in defining actin cytoskeletal assembly and Ca^{2+}-based thin filament regulation (el-Saleh et al., 1986).

Quantification of the overall gene expression levels of the four MHC isoforms (Figure 3A) show that TA is predominantly expressing Myh4, with lower levels of Myh1 and Myh2. However, SOL predominantly expresses Myh7 along with lower levels of Myh2 and Myh1. At the protein scale, both TA and SOL express varied myosin isoforms (Figure 3C). There are only fast isoforms in TA (~2/3 fast MHC IIb and 1/3 fast MHC IIx), while SOL has a close to 50:50 mix of fast MHC IIa and slow MHC I isoforms (Figure 3B). Myosin protein levels measured here are consistent with previous studies showing that muscles with larger physiological cross-sectional area (PCSA) also tend to contain more fast fibers (Burkholder et al., 1994; Pellegrino et al., 2003). However, analysis of myosin isoform expression in mouse muscle during postnatal development has also demonstrated expression of low levels of fast MHC IIa (Agbulut et al., 2003). While we did not detect any MHC IIa via SDS PAGE, we did detect low levels of fast MHC IIa via western blotting (not shown) and Tag-Seq (Figure 3A). There is a large degree of variability regarding the correlation between expression levels of RNA and protein (Gry et al., 2009). Consistent with this previous observation, gene and protein expression levels were largely well-aligned for the MHC isoforms expressed in TA, despite no presence of fast MHC IIa at the protein scale. However, the gene expression levels for SOL were ~5-fold higher for Myh7 compared to Myh2, while the protein expression levels were close to equal. These comparative data highlight that transcription may not directly relate to protein translation levels in the muscle, necessitating measurement of both RNA and protein levels.

Expression of MHC isoforms has repeatedly been shown to influence muscle contractile properties (Bottinelli and Reggiani, 2000; Pellegrino et al., 2003; Reiser et al., 2009), and are also a major determinant of shortening velocity of single muscle fibers. Here, the ATP dependence of actin sliding velocity was determined using the *in vitro* motility assay (Figure 4A). The 6.6-fold higher K_m observed for TA when compared to SOL represents a significantly lower affinity for ATP by the fast MHC isoforms in TA, along with a faster ADP release rate, thereby requiring a higher ATP concentration to reach half-maximal activation but with faster sliding velocities (Canepari et al., 2012). Consistent with the exclusive expression of fast myosin isoforms (Figure 3), the velocity of actin sliding (V_{ACTIN}) at saturating ATP (1.0 mM) for TA (3.91 ± 0.04 µm/sec) was in agreement with the V_{ACTIN} measured for pure fast (MHC IIb) myosin (Pellegrino et al., 2003). In contrast, V_{ACTIN} for SOL was 1.14 ± 0.05 µm/sec, close to the actin sliding velocity of pure slow I myosin (Pellegrino et al., 2003), despite this muscle having an almost 50:50 mixture of fast IIa and slow I MHC isoforms. These results indicate that differences in

aggregate behavior of isoform distributions in specific muscles can be highly nonlinear, with the slow isoforms having a dominating influence on shortening velocities compared to the fast isoforms, as shown previously (Egan et al., 2017; Harris et al., 1994).

The aggregate differences observed at the *in vitro* scale translate to the whole muscle scale under the influence of active as well as passive muscle characteristics. At the actomyosin scale, slow myosin isoforms are capable of producing *greater* force than fast isoforms due to the prolonged attachment time of the slower isoforms (Cuda et al., 1997; Harris et al., 1994). This is consistent with the actin filament velocity we obtained for the mix of fast and slow isoforms found in SOL, being closer to what would be seen for pure slow myosin (Pellegrino et al., 2003). Despite the apparent higher force production for the SOL myosin ensemble, the muscle mass-specific force measured for SOL at the intact muscle scale was lower than for TA. While our force measurements are comparable to those taken previously for these muscles (Close, 1965; Sacco and Jones, 1992) it cannot be ruled out that our different methods for testing SOL (*in-vitro*) and TA (*in*-situ) affected our force measurements, despite that we maintained the same temperature across preparations. The observed cross-scale discrepancy may also result from the more pennate structure of TA, which would result in more myofibers, and hence myosins, per cross-sectional area as compared to a less pennate muscle like SOL. These results highlight the need to consider muscle architecture when extrapolating from molecular-to tissue-scale experiments, as performed here. A related limitation of our study, therefore, is that we did not convert force measurements to stress (F/PCSA) due to the highly variable PCSA measurements for these small muscles in the literature (see introduction).

Muscle force production is subject to change with respect to external factors. Most muscles rotate skeletal joints as they contract and therefore operate across varying muscle and sarcomere lengths. The link between joint range-of-motion and sarcomere length change may vary with activation level and can be relaxed by muscle fiber architecture and compliance. As muscle activation was reduced from tetanic to twitch, we observed a right-shift in optimal length by 8%, comparable to the 7% for mouse SOL and EDL (Askew and Marsh, 1997), and 5% (maximal to submaximal only) for rat MG (Tijs et al., 2021).

To gain a simplified understanding of, and compare the range of operating lengths where SOL and the more pennate TA produce near-maximal force, we measured the FL plateau-width (Figure 5B,C,D) (Winters et al., 2011). Despite fiber architectural differences, both muscles generated near-maximal force ($\geq$90% P_o) across a broad range of tetanic operating lengths ($\pm$10%L_o). The plateau-width at twitch activation was 8% narrower for both muscles, consistent with a previously reported plateau-width reduction from maximal to submaximal activation in the rat MG (Tijs et al., 2021). Greater excursion

abilities are commonly attributed to the in-series sarcomeres of relatively parallel-fibered muscles like SOL (Lieber and Ward, 2011; Winters et al., 2011) and consistent with the relatively low stiffness of SOL, compared to TA (Figure 6D), so we predicted a greater plateau-width for SOL than TA. However, at the organ scale, SOL attaches to the bones it moves with significantly less tendon than TA, where added series elastic compliance may further decouple the length-change of muscle fibers and sarcomeres from the excursion of skeletal joints (Konow et al., 2012). Due to muscle architectural differences, we acknowledge that lengthening both muscles by a percent of whole muscle length is unlikely to be representative of the changes occurring at the sarcomere level, and this difference may have caused some of the force-length differences observed. Overall, however, our results underscore that structural differences between SOL and TA transcend organizational scales to shape their respective functions in postural control (SOL) and limb-swing initiation (TA).

Understanding the differences in passive muscle properties between SOL and TA also requires insights from multiple organizational scales. Passive muscle properties are driven by a combination of muscle architecture, titin isoform expression and extracellular matrix (ECM) organization and can be tuned by varying titin isoform length and/or the prominence of the ECM. Our results show that SOL stiffness is 16-fold lower (Figure 6A, D) compared to TA. This is consistent with the longer titin PEVK region that is expressed in SOL muscles (Figure 6E). The PEVK region is the predominant region of alternative splicing in titin and is composed of two sequence motifs: the 28 amino acid PPAK motif and the variable length poly-E motif. The primary building block is the PPAK motif and the increased exons in the SOL muscle, as evidenced by the four regions of higher exon inclusion seen in Figure 6E, result in a longer expressed titin isoform in SOL compared to TA. Therefore, consistent with observed correlations between PEVK length and passive tension in previous studies (Li et al., 2012; Prado et al., 2005), the increased length of titin in SOL muscle likely underlies the muscle's low passive stiffness (Figure 6).

Muscle architecture also contributes to this difference as muscles such as TA with more pennate architecture typically have more prominent ECM, and therefore greater passive stiffness (Granzier and Irving, 1995; Purslow, 2020). Interestingly, our Tag-Seq data did not show significant differences in the transcript levels for the primary collagen genes between SOL and TA (92 ± 50 and 182 ± 99 respectively, values expressed in FPKM. However, increased ECM component in pennate muscles may be regulated at the translational or post-translational level.

Comparison of the force-velocity relationships (Figure 7A) also highlights the influence of the myosin isoform and architecture differences on shortening velocities. For example, peak unloaded shortening velocity (V_{MAX}) was greater for TA compared to SOL (6.7 ± 0.4 and 4.6 ± 0.5 L_o/s respectively). Our V_{MAX} measurements for SOL fell within the range measured previously (Asmussen and Maréchal, 1989; Holt and Askew, 2012) but we measured lower average V_{MAX} for TA than a previous study (Burkholder and Lieber, 1998). However, consistent with our whole muscle V_{MAX} measurements, myosin purified from TA muscle also exhibited a higher V_{ACTIN} when compared with myosin purified from SOL muscle. Interestingly, the 3.4-fold difference between TA and SOL V_{ACTIN} (V_{ACTIN} TA/ V_{ACTIN} SOL) was dampened to a ~1.6-fold difference in V_{MAX} at the whole muscle scale (Figure 7A); a depression that cannot directly be explained by measurement variability. Likely explanations for this difference include incomplete recruitment of all fibers during muscle contraction (Holt et al., 2014) and the presence of internal loads at the whole muscle scale (Ross et al., 2020) that are not present with the protein isolates used for the IVM assay. For instance, TA is more pennate than, and contains more ECM than SOL. Hence, TA would likely have a larger internal (inertial) load, which may dampen V_{MAX}. It is also interesting to speculate that fiber pennation may be reducing the myosin-based velocity vector for TA (as a function of the cosine of the pennation angle) thus further reducing V_{MAX}, compared to SOL.

The curvature of the Hill-fit (Hill, 1938) applied to the muscle's force-velocity relationship (a/P_o) was greater for SOL than for TA (Figure 7D), indicating that shortening velocity is more load-sensitive for SOL than TA. Previous studies have shown that load slows ADP release in striated muscle myosins, which would ultimately decrease cross-bridge detachment rate and thus fiber shortening velocity under load (Greenberg et al., 2014; Newhard et al., 2019; Weiss et al., 2001). Because slow myosins are more sensitive to load and mouse SOL has a 50:50 mix of slow MHC I and fast MHC IIb myosin, it is likely that the slow myosin isoform expression contributes to the increased force-velocity curvature.

The application of load to the ADP binding pocket of myosin, is also influenced by differences in myosin light chain phosphorylation, which directly affects the load dependence of ADP release (Greenberg et al., 2009) as well as the loaded shortening velocities for MHC I (Greenberg et al., 2010; Karabina et al., 2015). Given the importance of the myosin light chains in supporting and stiffening the elongated alpha-helical neck region of myosin, it is interesting to speculate that the higher expression of Myl3 (Figure 2C) may play a role in the increased sensitivity to load in SOL myosin.

By contrast, TA shows a more consistent increase in velocity over all loads applied and therefore increased power compared to SOL. The right-ward shift in peak power towards faster shortening velocities for TA compared to SOL (Figure 7B) illustrates the functional effects on increased fast myosin expression (Figure 3C), consistent with the propensity for TA to prioritize power over force production (HILL, 1950). This propensity benefits TA during metabolically costly activities such as toe-off during running, compared to the lower energy consuming and slower contracting activities of SOL, the predominant role of which is postural maintenance.

Virtues of multi-scale research approaches

Skeletal muscle is often likened to a physiological "black box" because of its multi-scale organization and function. Prevalent views of muscle as either diverse or constrained in its structure-function have prevailed in disciplines operating at different scales for decades. We propose that these divergent views are predominantly shaped by a lack of cross-scale research interaction. Twenty-First Century convergence approaches can now let us *crack the code* of several biological black boxes, including muscle (e.g., (Cavigelli et al., 2021)). The utility of multi-scale approaches, as we have applied them here, likely extend to other areas in biology with complex interactions, ranging from microbial networks to ecosystem interactions. For muscle in particular, we anticipate leveraging the carefully characterized muscle types we have presented here and our multi-scale toolkit to determine e.g., how and why muscles with different fiber-type composition and architecture show different patterns of recovery from stretch injury and respond in different ways to changes in dietary nutrients.

CONCLUSIONS

Our integrative approach to studying muscles with disparate function identified the influence of myosin isoform distributions in determining muscle functional performance, along with additional, functionally relevant traits across scales of biological organization. We provide a comprehensive view of variations from gene expression to the protein scale, with respect to myosin isoform distributions, in addition to differences in gene expression signatures of associated proteins including titin, ECM, and actin regulatory and cytoskeletal proteins. Apart from major differences in myosin isoform distribution at the protein scale, our analyses of the contributions of specific muscle architecture, as it relates to structural properties of protein-protein interactions provide a deeper understanding of the cumulative effect of structural and functional traits in shaping overall muscle function. This understanding also highlights the need for interdisciplinary approaches. A deeper understanding of the multi-scale traits that shape muscle form and function will require an interdisciplinary toolkit but will also advance clinical and therapeutic efforts to

harness the regenerative properties of skeletal muscle and extend its functionality beyond exercise injury, myopathies, and into older age of our longer-living population.

ACKNOWLEDGEMENTS

We thank Eric Hardiman, Krina Shah, Magdolin Shenouda, and Devin Jenness for assistance with muscle experiments, and Jack Lepine for sequencing assistance. Thanks to students in the 2020 Biology of Muscle course at UML for tracking actin filaments. Andrew Biewener and the Concord Field Station (Harvard University) were generous with facilities and resources, and Pedro Ramirez's animal care was invaluable. Two anonymous reviewers provided comments to improve our manuscript. This is publication #5 for the UMass Movement Center (UMOVE).

COMPETING INTERESTS

No competing interests declared.

FUNDING

This work was supported by NIH grants R01HL123774 to JRM and AHA grant 20PRE35120307 to SS, seed awards from UML (to NK #R50180000038587; to MG #R51080000038586), and startup-funding from UMass Lowell to NK.

DATA AVAILABILITY

Muscle and protein data pertaining to these analyses will be lodged in Dryad upon acceptance of this manuscript. Tag-seq data will be uploaded to GEO upon acceptance of this manuscript.

AUTHOR CONTRIBUTIONS

Study conceptualization: NK, JM, MG. Execution of experiments: BR, SS, NL, AR, PH, SD, AS, NK. Data conditioning and analyses: BR, PM, SS, NL, AR, PH, SD, NK. Manuscript draft: SS, BR, JM, NK. Manuscript editing and approval: all authors.

REFERENCES

Agbulut, O., Noirez, P., Beaumont, F., Butler-Browne, G., 2003. Myosin heavy chain isoforms in postnatal muscle development of mice. Biol Cell 95, 399–406. https://doi.org/10.1016/s0248-4900(03)00087-x

Askew, G.N., Marsh, R.L., 1997. The effects of length trajectory on the mechanical power output of mouse skeletal muscles. J Exp Biol 200, 3119–3131.

Askew, G.N., Young, I.S., Altringham, J.D., 1997. Fatigue of mouse soleus muscle, using the work loop technique. J Exp Biol 200, 2907–2912.

Asmussen, G., Maréchal, G., 1989. Maximal shortening velocities, isomyosins and fibre types in soleus muscle of mice, rats and guinea-pigs. J Physiol 416, 245–254. https://doi.org/10.1113/jphysiol.1989.sp017758

Bárány, M., 1967. ATPase activity of myosin correlated with speed of muscle shortening. J Gen Physiol 50, Suppl:197-218. https://doi.org/10.1085/jgp.50.6.197

Blough, E.R., Rennie, E.R., Zhang, F., Reiser, P.J., 1996. Enhanced electrophoretic separation and resolution of myosin heavy chains in mammalian and avian skeletal muscles. Anal Biochem 233, 31–35. https://doi.org/10.1006/abio.1996.0003

Boss, A., Heskamp, L., Breukels, V., Bains, L.J., van Uden, M.J., Heerschap, A., 2018. Oxidative capacity varies along the length of healthy human tibialis anterior. J Physiol 596, 1467–1483. https://doi.org/10.1113/JP275009

Bottinelli, R., Reggiani, C., 2000. Human skeletal muscle fibres: molecular and functional diversity. Prog Biophys Mol Biol 73, 195–262. https://doi.org/10.1016/s0079-6107(00)00006-7

Bottinelli, R., Schiaffino, S., Reggiani, C., 1991. Force-velocity relations and myosin heavy chain isoform compositions of skinned fibres from rat skeletal muscle. J Physiol 437, 655–672. https://doi.org/10.1113/jphysiol.1991.sp018617

Brooks, S.V., Faulkner, J.A., 1988. Contractile properties of skeletal muscles from young, adult and aged mice. The Journal of Physiology 404, 71–82. https://doi.org/10.1113/jphysiol.1988.sp017279

Burke, R.E., Levine, D.N., Zajac, F.E., 1971. Mammalian motor units: physiological-histochemical correlation in three types in cat gastrocnemius. Science 174, 709–712. https://doi.org/10.1126/science.174.4010.709

Burkholder, T.J., Fingado, B., Baron, S., Lieber, R.L., 1994. Relationship between muscle fiber types and sizes and muscle architectural properties in the mouse hindlimb. J Morphol 221, 177–190. https://doi.org/10.1002/jmor.1052210207

Burkholder, T.J., Lieber, R.L., 1998. Sarcomere number adaptation after retinaculum transection in adult mice. J Exp Biol 201, 309–316.

Canepari, M., Maffei, M., Longa, E., Geeves, M., Bottinelli, R., 2012. Actomyosin kinetics of pure fast and slow rat myosin isoforms studied by in vitro motility assay approach. Exp Physiol 97, 873–881. https://doi.org/10.1113/expphysiol.2012.064576

Cavigelli, S., Leips, J., Jenny Xiang, Q.-Y., Lemke, D., Konow, N., 2021. Next Steps in Integrative Biology: Mapping Interactive Processes Across Levels of Biological Organization. Integr Comp Biol icab161. https://doi.org/10.1093/icb/icab161

Charles, J.P., Cappellari, O., Spence, A.J., Hutchinson, J.R., Wells, D.J., 2016. Musculoskeletal Geometry, Muscle Architecture and Functional Specialisations of the Mouse Hindlimb. PLoS One 11, e0147669. https://doi.org/10.1371/journal.pone.0147669

Close, R., 1965. Force: velocity properties of mouse muscles. Nature 206, 718–719. https://doi.org/10.1038/206718a0

Close, R., 1964. DYNAMIC PROPERTIES OF FAST AND SLOW SKELETAL MUSCLES OF THE RAT DURING DEVELOPMENT. J Physiol 173, 74–95. https://doi.org/10.1113/jphysiol.1964.sp007444

Cuda, G., Pate, E., Cooke, R., Sellers, J.R., 1997. In vitro actin filament sliding velocities produced by mixtures of different types of myosin. Biophys J 72, 1767–1779. https://doi.org/10.1016/S0006-3495(97)78823-4

Daut, J., Elzinga, G., 1989. Substrate dependence of energy metabolism in isolated guinea-pig cardiac muscle: a microcalorimetric study. J Physiol 413, 379–397. https://doi.org/10.1113/jphysiol.1989.sp017659

Eckels, E.C., Tapia-Rojo, R., Rivas-Pardo, J.A., Fernández, J.M., 2018. The Work of Titin Protein Folding as a Major Driver in Muscle Contraction. Annu Rev Physiol 80, 327–351. https://doi.org/10.1146/annurev-physiol-021317-121254

Egan, P.F., Moore, J.R., Ehrlicher, A.J., Weitz, D.A., Schunn, C., Cagan, J., LeDuc, P., 2017. Robust mechanobiological behavior emerges in heterogeneous myosin systems. Proc Natl Acad Sci U S A 114, E8147–E8154. https://doi.org/10.1073/pnas.1713219114

el-Saleh, S.C., Warber, K.D., Potter, J.D., 1986. The role of tropomyosin-troponin in the regulation of skeletal muscle contraction. J Muscle Res Cell Motil 7, 387–404. https://doi.org/10.1007/BF01753582

Freiburg, A., Trombitas, K., Hell, W., Cazorla, O., Fougerousse, F., Centner, T., Kolmerer, B., Witt, C., Beckmann, J.S., Gregorio, C.C., Granzier, H., Labeit, S., 2000. Series of exon-skipping events in the elastic spring region of titin as the structural basis for myofibrillar elastic diversity. Circ Res 86, 1114–1121. https://doi.org/10.1161/01.res.86.11.1114

Granzier, H.L., Irving, T.C., 1995. Passive tension in cardiac muscle: contribution of collagen, titin, microtubules, and intermediate filaments. Biophys J 68, 1027–1044. https://doi.org/10.1016/S0006-3495(95)80278-X

Greenberg, M.J., Kazmierczak, K., Szczesna-Cordary, D., Moore, J.R., 2010. Cardiomyopathy-linked myosin regulatory light chain mutations disrupt myosin strain-dependent biochemistry. Proc. Natl. Acad. Sci. U.S.A. 107, 17403–17408. https://doi.org/10.1073/pnas.1009619107

Greenberg, M.J., Mealy, T.R., Watt, J.D., Jones, M., Szczesna-Cordary, D., Moore, J.R., 2009. The molecular effects of skeletal muscle myosin regulatory light chain phosphorylation. Am J Physiol Regul Integr Comp Physiol 297, R265-274. https://doi.org/10.1152/ajpregu.00171.2009

Greenberg, M.J., Shuman, H., Ostap, E.M., 2014. Inherent force-dependent properties of β-cardiac myosin contribute to the force-velocity relationship of cardiac muscle. Biophys J 107, L41–L44. https://doi.org/10.1016/j.bpj.2014.11.005

Gry, M., Rimini, R., Strömberg, S., Asplund, A., Pontén, F., Uhlén, M., Nilsson, P., 2009. Correlations between RNA and protein expression profiles in 23 human cell lines. BMC Genomics 10, 365. https://doi.org/10.1186/1471-2164-10-365

Hakim, C.H., Wasala, N.B., Duan, D., 2013. Evaluation of muscle function of the extensor digitorum longus muscle ex vivo and tibialis anterior muscle in situ in mice. J Vis Exp 50183. https://doi.org/10.3791/50183

Harris, D.E., Work, S.S., Wright, R.K., Alpert, N.R., Warshaw, D.M., 1994. Smooth, cardiac and skeletal muscle myosin force and motion generation assessed by cross-bridge mechanical interactions in vitro. J Muscle Res Cell Motil 15, 11–19. https://doi.org/10.1007/BF00123828

Heemskerk, A.M., Strijkers, G.J., Vilanova, A., Drost, M.R., Nicolay, K., 2005. Determination of mouse skeletal muscle architecture using three-dimensional diffusion tensor imaging. Magnetic Resonance in Medicine 53, 1333–1340. https://doi.org/10.1002/mrm.20476

Hettige, P., Tahir, U., Nishikawa, K.C., Gage, M.J., 2020. Comparative analysis of the transcriptomes of EDL, psoas, and soleus muscles from mice. BMC Genomics 21, 808. https://doi.org/10.1186/s12864-020-07225-2

HILL, A.V., 1950. THE DIMENSIONS OF ANIMALS AND THEIR MUSCULAR DYNAMICS. Science Progress (1933-) 38, 209–230.

Hill, A.V., 1938. The heat of shortening and the dynamic constants of muscle. Proceedings of the Royal Society of London. Series B - Biological Sciences 126, 136–195. https://doi.org/10.1098/rspb.1938.0050

Holt, N.C., Askew, G.N., 2012. The effects of asymmetric length trajectories on the initial mechanical efficiency of mouse soleus muscles. J Exp Biol 215, 324–330. https://doi.org/10.1242/jeb.062703

Holt, N.C., Wakeling, J.M., Biewener, A.A., 2014. The effect of fast and slow motor unit activation on whole-muscle mechanical performance: the size principle may not pose a mechanical paradox. Proc Biol Sci 281, 20140002. https://doi.org/10.1098/rspb.2014.0002

Höök, P., Li, X., Sleep, J., Hughes, S., Larsson, L., 1999. In vitro motility speed of slow myosin extracted from single soleus fibres from young and old rats. J Physiol 520 Pt 2, 463–471. https://doi.org/10.1111/j.1469-7793.1999.00463.x

Horak, M., Novak, J., Bienertova-Vasku, J., 2016. Muscle-specific microRNAs in skeletal muscle development. Dev Biol 410, 1–13. https://doi.org/10.1016/j.ydbio.2015.12.013

Huxley, A.F., 1957. Muscle structure and theories of contraction. Prog Biophys Biophys Chem 7, 255–318.

Huxley, A.F., Niedergerke, R., 1954. Structural changes in muscle during contraction; interference microscopy of living muscle fibres. Nature 173, 971–973. https://doi.org/10.1038/173971a0

Huxley, H., Hanson, J., 1954. Changes in the cross-striations of muscle during contraction and stretch and their structural interpretation. Nature 173, 973–976.

Jackson, D.A., 1993. Stopping Rules in Principal Components Analysis: A Comparison of Heuristical and Statistical Approaches. Ecology 74, 2204–2214. https://doi.org/10.2307/1939574

James, R.S., Altringham, J.D., Goldspink, D.F., 1995. The mechanical properties of fast and slow skeletal muscles of the mouse in relation to their locomotory function. J Exp Biol 198, 491–502.

Karabina, A., Kazmierczak, K., Szczesna-Cordary, D., Moore, J.R., 2015. Myosin regulatory light chain phosphorylation enhances cardiac β-myosin in vitro motility under load. Arch. Biochem. Biophys. 580, 14–21. https://doi.org/10.1016/j.abb.2015.06.014
Konow, N., Azizi, E., Roberts, T.J., 2012. Muscle power attenuation by tendon during energy dissipation. Proc Biol Sci 279, 1108–1113. https://doi.org/10.1098/rspb.2011.1435
Lal, N.N., Cornwall, J., Sheard, P.W., 2021. Age-related structural changes show that loss of fibers is not a significant contributor to muscle atrophy in old mice. Experimental Gerontology 156, 111618. https://doi.org/10.1016/j.exger.2021.111618
Li, S., Guo, W., Schmitt, B.M., Greaser, M.L., 2012. Comprehensive analysis of titin protein isoform and alternative splicing in normal and mutant rats. J Cell Biochem 113, 1265–1273. https://doi.org/10.1002/jcb.23459
Lieber, R.L., Fridén, J., 2000. Functional and clinical significance of skeletal muscle architecture. Muscle Nerve 23, 1647–1666. https://doi.org/10.1002/1097-4598(200011)23:11<1647::aid-mus1>3.0.co;2-m
Lieber, R.L., Ward, S.R., 2011. Skeletal muscle design to meet functional demands. Philos Trans R Soc Lond B Biol Sci 366, 1466–1476. https://doi.org/10.1098/rstb.2010.0316
Linke, W.A., Ivemeyer, M., Olivieri, N., Kolmerer, B., Rüegg, J.C., Labeit, S., 1996. Towards a molecular understanding of the elasticity of titin. J Mol Biol 261, 62–71. https://doi.org/10.1006/jmbi.1996.0441
Lovering, R.M., Shah, S.B., Pratt, S.J.P., Gong, W., Chen, Y., 2013. Architecture of healthy and dystrophic muscles detected by optical coherence tomography. Muscle & Nerve 47, 588–590. https://doi.org/10.1002/mus.23711
Lutz, G.J., Bremner, S.N., Bade, M.J., Lieber, R.L., 2001. Identification of myosin light chains in Rana pipiens skeletal muscle and their expression patterns along single fibres. J Exp Biol 204, 4237–4248.
Malmqvist, U.P., Aronshtam, A., Lowey, S., 2004. Cardiac myosin isoforms from different species have unique enzymatic and mechanical properties. Biochemistry 43, 15058–15065. https://doi.org/10.1021/bi0495329
Moo, E.K., Fortuna, R., Sibole, S.C., Abusara, Z., Herzog, W., 2016. In vivo Sarcomere Lengths and Sarcomere Elongations Are Not Uniform across an Intact Muscle. Frontiers in Physiology 7.
Moran, A.L., Warren, G.L., Lowe, D.A., 2005. Soleus and EDL muscle contractility across the lifespan of female C57BL/6 mice. Exp Gerontol 40, 966–975. https://doi.org/10.1016/j.exger.2005.09.005
Narici, M., Franchi, M., Maganaris, C., 2016. Muscle structural assembly and functional consequences. J Exp Biol 219, 276–284. https://doi.org/10.1242/jeb.128017
Newhard, C.S., Walcott, S., Swank, D.M., 2019. The load dependence of muscle's force-velocity curve is modulated by alternative myosin converter domains. Am J Physiol Cell Physiol 316, C844–C861. https://doi.org/10.1152/ajpcell.00494.2018
Orzechowski, M., Fischer, S., Moore, J.R., Lehman, W., Farman, G.P., 2014. Energy landscapes reveal the myopathic effects of tropomyosin mutations. Arch. Biochem. Biophys. 564, 89–99. https://doi.org/10.1016/j.abb.2014.09.007

Pellegrino, M.A., Canepari, M., Rossi, R., D'Antona, G., Reggiani, C., Bottinelli, R., 2003. Orthologous myosin isoforms and scaling of shortening velocity with body size in mouse, rat, rabbit and human muscles. J Physiol 546, 677–689. https://doi.org/10.1113/jphysiol.2002.027375

Pette, D., Staron, R.S., 2000. Myosin isoforms, muscle fiber types, and transitions. Microsc Res Tech 50, 500–509. https://doi.org/10.1002/1097-0029(20000915)50:6<500::AID-JEMT7>3.0.CO;2-7

Prado, L.G., Makarenko, I., Andresen, C., Krüger, M., Opitz, C.A., Linke, W.A., 2005. Isoform diversity of giant proteins in relation to passive and active contractile properties of rabbit skeletal muscles. J Gen Physiol 126, 461–480. https://doi.org/10.1085/jgp.200509364

Purslow, P.P., 2020. The Structure and Role of Intramuscular Connective Tissue in Muscle Function. Front Physiol 11, 495. https://doi.org/10.3389/fphys.2020.00495

Rassier, D.E., MacIntosh, B.R., Herzog, W., 1999. Length dependence of active force production in skeletal muscle. J Appl Physiol (1985) 86, 1445–1457. https://doi.org/10.1152/jappl.1999.86.5.1445

Reiser, P.J., Bicer, S., Chen, Q., Zhu, L., Quan, N., 2009. Masticatory (;superfast') myosin heavy chain and embryonic/atrial myosin light chain 1 in rodent jaw-closing muscles. J Exp Biol 212, 2511–2519. https://doi.org/10.1242/jeb.031369

Ross, S.A., Rimkus, B., Konow, N., Biewener, A.A., Wakeling, J.M., 2020. Added mass in rat plantaris muscle causes a reduction in mechanical work. J Exp Biol 223, jeb224410. https://doi.org/10.1242/jeb.224410

Sacco, P., Jones, D.A., 1992. The protective effect of damaging eccentric exercise against repeated bouts of exercise in the mouse tibialis anterior muscle. Exp Physiol 77, 757–760. https://doi.org/10.1113/expphysiol.1992.sp003642

Schafer, S., Miao, K., Benson, C.C., Heinig, M., Cook, S.A., Hubner, N., 2015. Alternative Splicing Signatures in RNA-seq Data: Percent Spliced in (PSI). Curr Protoc Hum Genet 87, 11.16.1-11.16.14. https://doi.org/10.1002/0471142905.hg1116s87

Schiaffino, S., Reggiani, C., 2011. Fiber types in mammalian skeletal muscles. Physiol Rev 91, 1447–1531. https://doi.org/10.1152/physrev.00031.2010

Schiaffino, S., Reggiani, C., 1994. Myosin isoforms in mammalian skeletal muscle. J Appl Physiol (1985) 77, 493–501. https://doi.org/10.1152/jappl.1994.77.2.493

Sitbon, Y.H., Diaz, F., Kazmierczak, K., Liang, J., Wangpaichitr, M., Szczesna-Cordary, D., 2021. Cardiomyopathic mutations in essential light chain reveal mechanisms regulating the super relaxed state of myosin. J Gen Physiol 153, e202012801. https://doi.org/10.1085/jgp.202012801

Spudich, J.A., Watt, S., 1971. The regulation of rabbit skeletal muscle contraction. I. Biochemical studies of the interaction of the tropomyosin-troponin complex with actin and the proteolytic fragments of myosin. J. Biol. Chem. 246, 4866–4871.

Stål, P., Eriksson, P.O., Schiaffino, S., Butler-Browne, G.S., Thornell, L.E., 1994. Differences in myosin composition between human oro-facial, masticatory and limb muscles: enzyme-, immunohisto- and biochemical studies. J Muscle Res Cell Motil 15, 517–534. https://doi.org/10.1007/BF00121158

Staron, R.S., Johnson, P., 1993. Myosin polymorphism and differential expression in adult human skeletal muscle. Comp Biochem Physiol B 106, 463–475. https://doi.org/10.1016/0305-0491(93)90120-t

Sundar, S., Rynkiewicz, M.J., Ghosh, A., Lehman, W., Moore, J.R., 2020. Cardiomyopathy Mutation Alters End-to-End Junction of Tropomyosin and Reduces Calcium Sensitivity. Biophys. J. 118, 303–312. https://doi.org/10.1016/j.bpj.2019.11.3396

Terry, E.E., Zhang, X., Hoffmann, C., Hughes, L.D., Lewis, S.A., Li, J., Wallace, M.J., Riley, L.A., Douglas, C.M., Gutierrez-Monreal, M.A., Lahens, N.F., Gong, M.C., Andrade, F., Esser, K.A., Hughes, M.E., 2018. Transcriptional profiling reveals extraordinary diversity among skeletal muscle tissues. Elife 7, e34613. https://doi.org/10.7554/eLife.34613

Tijs, C., Konow, N., Biewener, A.A., 2021. Effect of muscle stimulation intensity on the heterogeneous function of regions within an architecturally complex muscle. J Appl Physiol (1985) 130, 941–951. https://doi.org/10.1152/japplphysiol.00514.2020

Trombitás, K., Greaser, M., Labeit, S., Jin, J.P., Kellermayer, M., Helmes, M., Granzier, H., 1998. Titin extensibility in situ: entropic elasticity of permanently folded and permanently unfolded molecular segments. J Cell Biol 140, 853–859. https://doi.org/10.1083/jcb.140.4.853

Weiss, S., Rossi, R., Pellegrino, M.A., Bottinelli, R., Geeves, M.A., 2001. Differing ADP release rates from myosin heavy chain isoforms define the shortening velocity of skeletal muscle fibers. J Biol Chem 276, 45902–45908. https://doi.org/10.1074/jbc.M107434200

Wells, J.B., 1965. COMPARISON OF MECHANICAL PROPERTIES BETWEEN SLOW AND FAST MAMMALIAN MUSCLES. J Physiol 178, 252–269. https://doi.org/10.1113/jphysiol.1965.sp007626

Westerblad, H., Bruton, J.D., Katz, A., 2010. Skeletal muscle: energy metabolism, fiber types, fatigue and adaptability. Exp Cell Res 316, 3093–3099. https://doi.org/10.1016/j.yexcr.2010.05.019

Wilkie, D.R., 1949. The relation between force and velocity in human muscle. J Physiol 110, 249–280.

Winters, T.M., Takahashi, M., Lieber, R.L., Ward, S.R., 2011. Whole muscle length-tension relationships are accurately modeled as scaled sarcomeres in rabbit hindlimb muscles. J Biomech 44, 109–115. https://doi.org/10.1016/j.jbiomech.2010.08.033

Figures

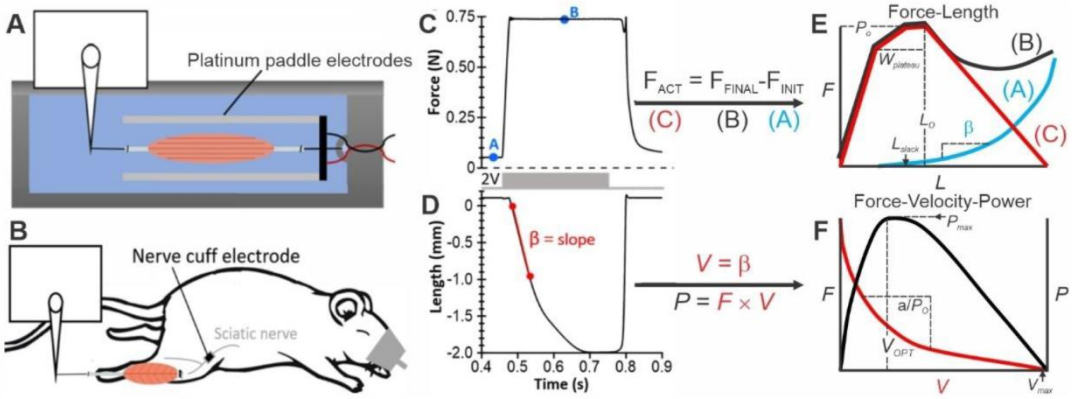

Figure 1: Ergometry approach. (A) SOL tested *in vitro* in Ringer's bath. (B) TA tested *in situ* with prep viability maintained by cardiovascular supply from mouse. (C) and (D) show example data traces for a force-velocity trial and the measurements extracted to generate summary curves. (E) and (F) show measurement extraction for Force-Length (Figure 5 and 6), and Force-Velocity-Power (Figure 7) respectively. L_o, optimal length; L_{slack}, muscle slack-length; P_o, peak isometric force; $W_{plateau}$, FL plateau width; β, passive muscle stiffness; V_{max}, peak contraction velocity; V_{opt}, velocity of peak power production; P_{max}, peak power; a/P_o, force-velocity curvature.

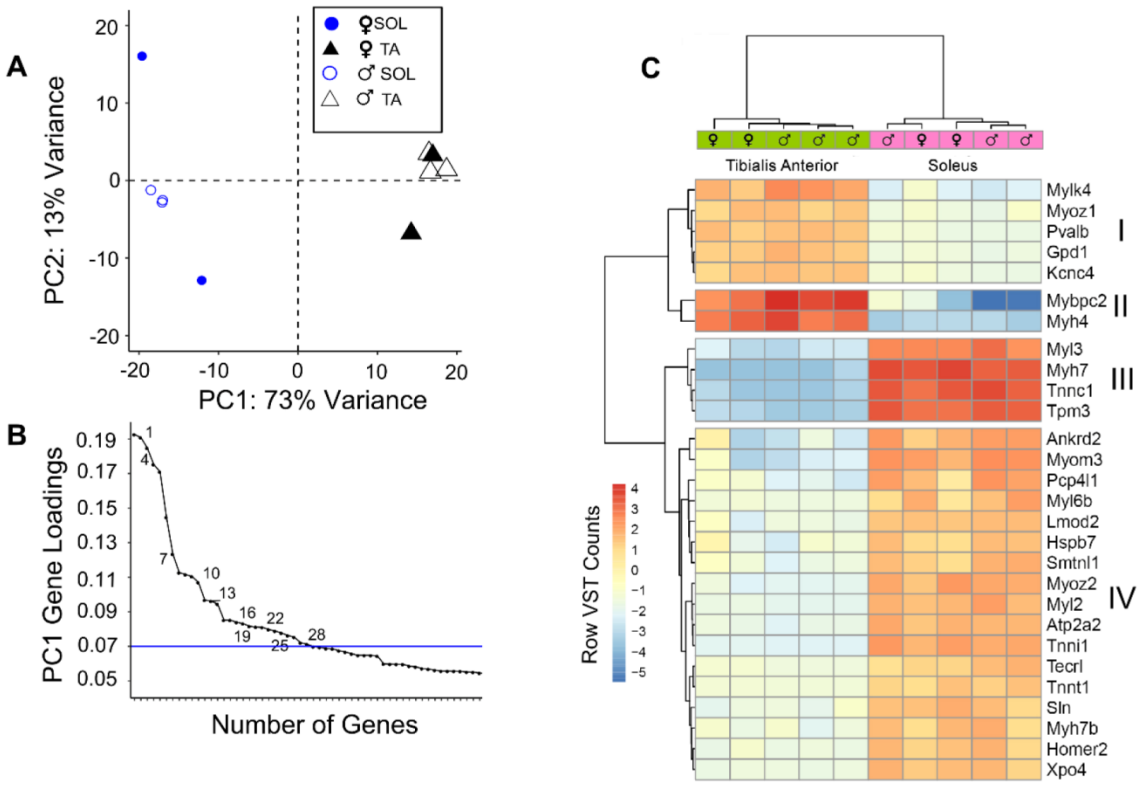

Figure 2: Transcriptomic signatures of SOL and TA. (A) Topological distribution of the biological replicates of SOL and TA create two distinct clusters across the first two principal components (PC) calculated for the differentially expressed genes. (B) Differentially expressed genes ranked by PC1 feature loading. The blue horizontal line indicates the cutoff value (0.07) which was utilized to extract the genes with strongest contribution to PC1. (C) Heat map visualizing the level of relative up (red) or down (blue) regulation of selected genes in SOL and TA samples (Supplementary Table 1). Columns represent biological replicates, rows represent genes. Color intensity in each sample is proportional to the expression deviation from the mean normalized count of the gene.

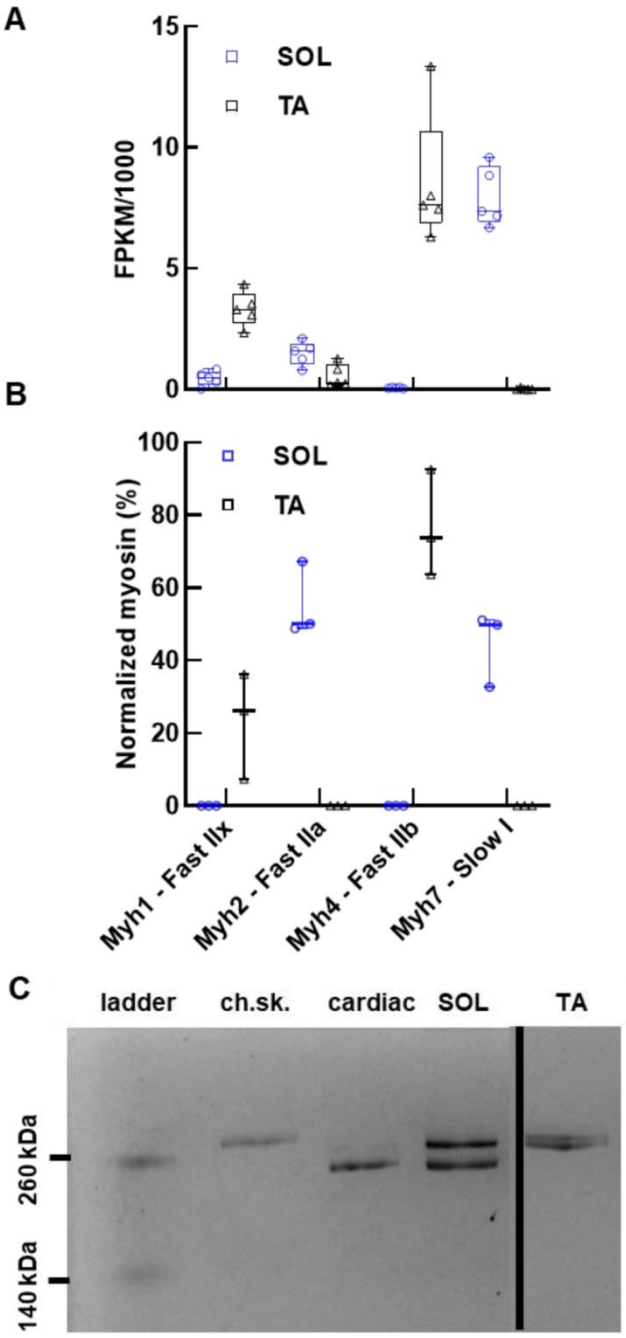

Figure 3: Slow myosin expression is exclusively found in SOL. (A) Expression levels of the four Myosin isoforms in TA and Soleus shown in Fragments per kilobase million (FPKM). The slow isoform Myh7 was expressed more in the Soleus samples while the fast isoform Myh4 and Myh1 are primarily expressed in the TA samples. (N = 5 SOL, N = 5 TA). (B) Myosin isoform distribution quantified from SDS-PAGE myosin gel using densitometric analysis in Image J, shows TA with only fast isoforms (IIx and IIb) and SOL with mixture of fast (IIa) and slow (I); n = 3/muscle. Same x-axis labels in A and B

panels represent different myosin isoforms. (C) An unaltered representative image of the SDS-PAGE myosin gel (8% with 35% glycerol) with chicken pectoralis (ch.sk.), mouse cardiac, Soleus (SOL), TA samples.

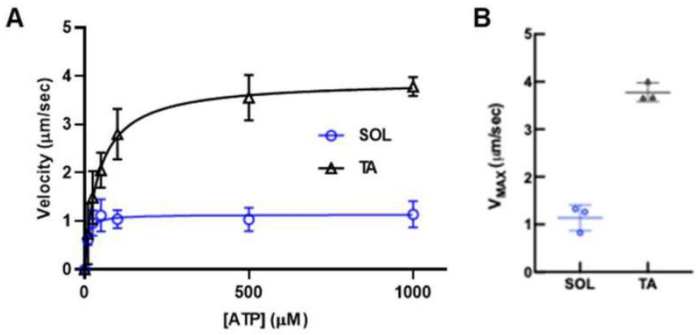

Figure 4: Mean actin sliding velocity from purified naïve SOL and TA myosin using in-vitro motility assay. (A) ATP dependence of actin sliding velocity (0 µM to 1 mM), fit to Michaelis-Menten equation, shows different mean actin sliding velocities (Vactin) and Km (SOL: open blue circles; TA: open black triangles). (B) Mean actin sliding velocity at 1 mM ATP depicts a 3.3-fold difference between TA and SOL myosin. Data is average of three technical repeats (respective myosin purified from 5 mice muscle pairs), with error bars representing the standard deviation (SD).

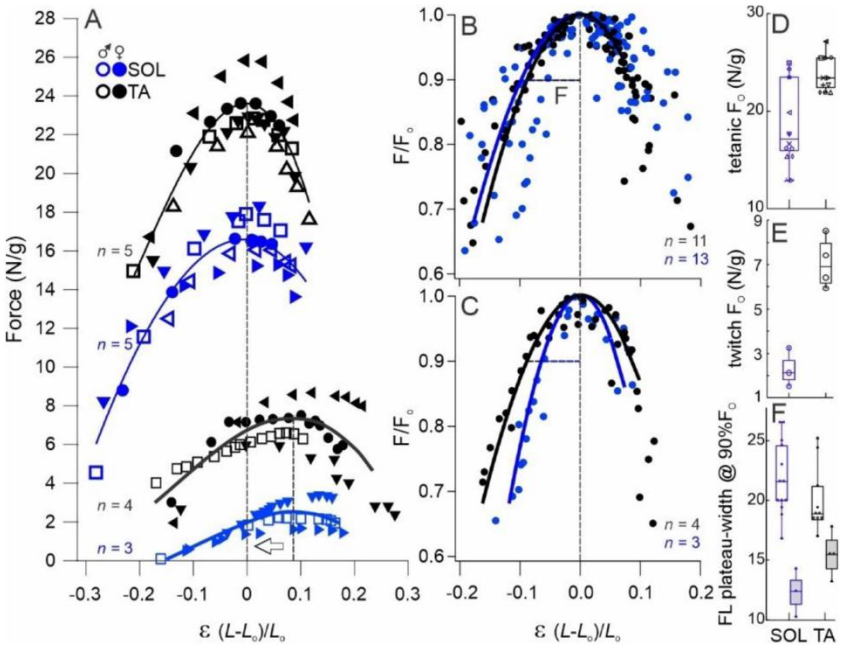

Figure 5: Comparison of active force-length properties for SOL (blue) and TA (black). (A) Muscle mass-specific force (y-axis) plotted against strain (muscle length normalized to tetanic L_o; x-axis) for tetanic and twitch contractions. Symbols delineate subjects; solid/thick symbols = females; open/thin symbols = males. Note that L_o is left-shifted by approx. 8% as activation increases (white arrow, see results for details). (B-C). Plateau width for the ascending limb, measured at 90%P_o for (B) tetanic, and (C) twitch contractions. (D-F). Box-plots showing summary median-quartile and range data with individual measurements indicated by symbols for (D) muscle mass-specific tetanic force. (E) muscle mass-specific twitch force. (F) The ascending plateau-width at 90% P_o for the active tetanic (unfilled boxes) and twitch (grey-filled boxes) FL curves. All summary variable comparisons between SOL and TA, except in F, are statistically significantly different ($p<0.01$; see text for GLM model details). Muscle sample sizes are shown next to curves.

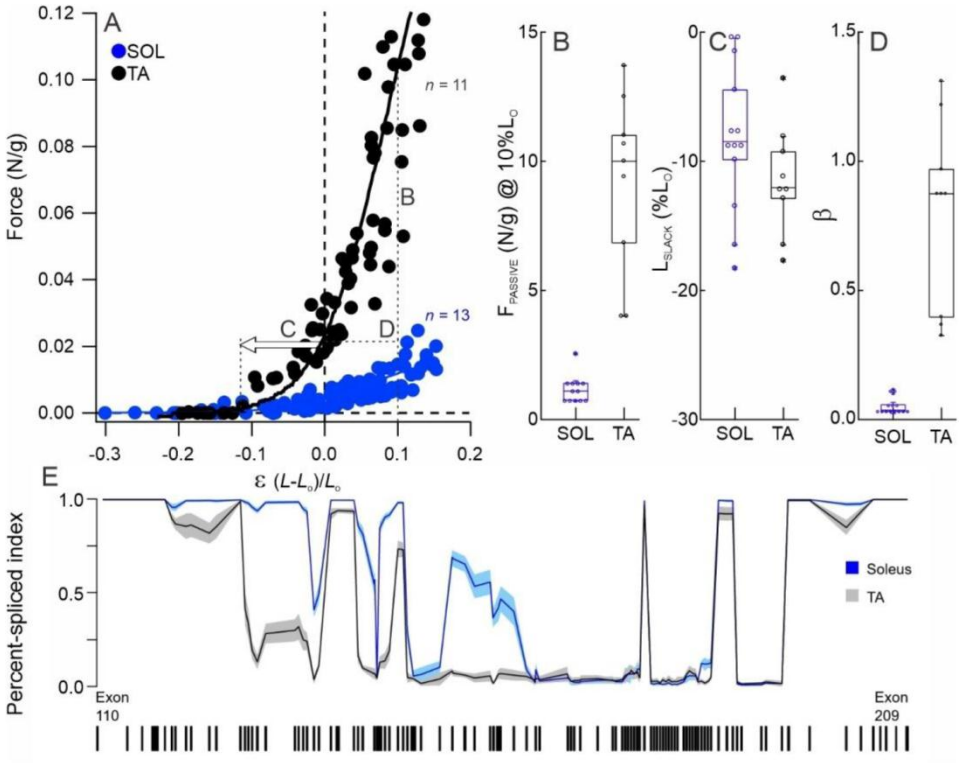

Figure 6. Comparison of passive force-length properties for SOL (blue) and TA (black). (A) Muscle mass-specific passive force (y-axis) plotted against strain (muscle length normalized to tetanic L_o; x-axis). (B-D) Box-plots showing summary median-quartile and range data with individual measurements indicated by symbols for (B) muscle slack-length, (C) Passive force at 10% beyond L_o, and (D) slope of the passive FL relationship, measured from L_o to 110% L_o, representing the relative difference in stiffness of the two muscles. (E) Percent Spliced Index plot for the PEVK regions of SOL and TA titin, showing the mean PSI values for six biological replicates of either TA or SOL with the shaded regions representing the standard deviation in the PSI values. The relatively lower values for TA than SOL (1=100% inclusion; 0=complete exclusion of an exon from the transcript pool), suggest expression of shorter titin isoform(s) in TA (black) than SOL (blue). Exon numbering based on NCBI entry BN001114.1 and Ensemble titin transcript ENSMUST00000099981.9.

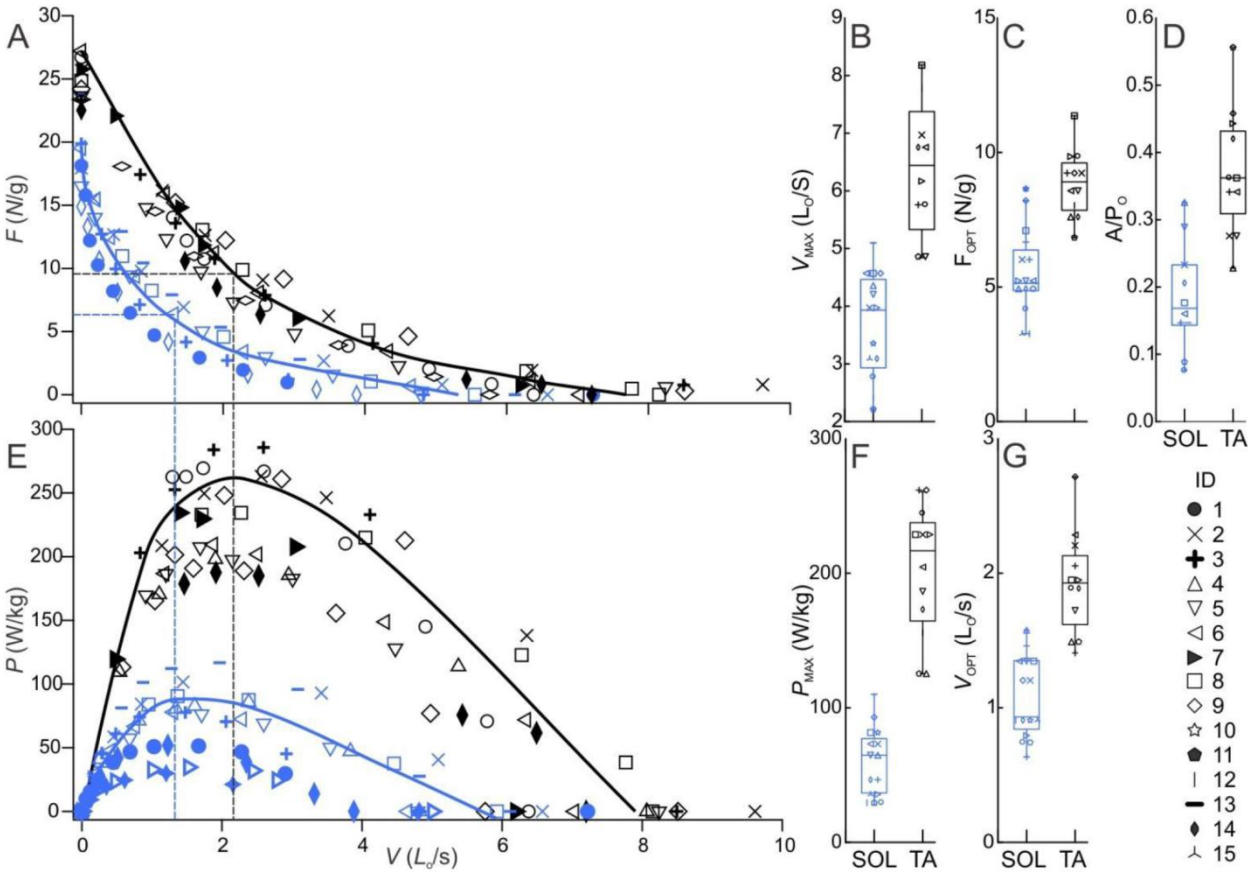

Figure 7: Comparison of force-velocity-power relationships for SOL (blue) and TA (black). (A) force-velocity relationships, normalized to muscle mass (N/g, y-axis) and optimal length (L_o, x-axis), respectively. Summary FV curves (bold lines) for each muscle from a custom-implementation of the Hill equation in Igor Pro. (B-D) Box-plots showing median-quartile and range data with individual measurements indicated by symbols, summarizing force-velocity data; (B) peak unloaded velocity, (C) force at optimal length (see dashed lines in A), and (D) FV curvature (lower values indicate more FV curvature). (E) power-velocity relationships, normalized to muscle mass and optimal length, respectively. (F) Muscle-mass-specific peak power, and (G) optimal velocity, where peak power occurs (dashed lines in B) Symbols delineate subjects; solid/thick symbols = females; open/thin symbols = males. All summary data comparisons between SOL and TA are statistically significantly different ($p<0.01$; see text for GLM model details).

Table S1. Gene symbol, name, and description along with gene regulation in SOL and TA. Upregulation (red) and down regulation (blue) as shown in the expression heatmap (Figure 2C).

Gene symbol	Gene Description	Gene ontology	TA	SOL
Mylk4	myosin light chain kinase family, member 4	protein serine/threonine kinase activity		
Myoz1	myozenin 1	muscle system process, striated muscle tissue development, actomyosin structure organization, second messenger mediated signaling, muscle cell differentiation, cellular component assembly involved in morphogenesis		
Pvalb	parvalbumin	actin cytoskeleton, stereocilium, stereocilium bundle, cortical cytoskeleton		
Gpd1	glycerol-3-phosphate dehydrogenase 1	glycerol-3-phosphate metabolic process, alditol phosphate metabolic process, positive regulation of glycolytic process		
Kcnc4	potassium voltage gated channel, Shaw-related subfamily, member 4	regulation of action potential, action potential, regulation of neurotransmitter secretion		
Mybpc 2	myosin binding protein C, fast-type	muscle contraction, myosin filament assembly, muscle tissue development, cellular component assembly involved in morphogenesis, cardiocyte differentiation, myosin filament organization, muscle organ morphogenesis, actomyosin structure, organization, muscle system process		
Myh4	myosin, heavy polypeptide 4, skeletal muscle	muscle system process, muscle contraction, response to activity, actin cytoskeleton, myofibril, contractile fiber, myosin complex, myosin filament, actin binding, actin filament binding, motor activity, calmodulin binding		

Myl3	myosin, light polypeptide 3	muscle system process, striated muscle tissue development, muscle organ morphogenesis, cardiac chamber development, regulation of the force of heart contraction, striated muscle contraction		
Myh7	myosin, heavy polypeptide 7	striated muscle tissue development, actin-mediated cell contraction, musculoskeletal movement, regulation of force of heart contraction, multicellular organismal movement, cardiac chamber development, muscle hypertrophy, actin filament-based movement, muscle tissue morphogenesis		
Tnnc1	troponin C, cardiac and slow skeletal	striated muscle tissue development, regulation of ATPase activity, actin-mediated cell contraction, musculoskeletal movement, multicellular organismal movement, muscle system process, muscle organ development, muscle adaptation, cardiac chamber development, heart contraction		
Tpm3	tropomyosin 3	actin filament organization, actin cytoskeleton, actin filament, stress fiber, contractile actin filament bundle, actin filament bundle, actomyosin, cortical cytoskeleton, actin binding		
Ankrd2	ankyrin repeat domain 2	muscle tissue development, skeletal muscle organ development		
Myom3	myomesin family, member 3	muscle contraction, myosin filament assembly, muscle tissue development, cellular component assembly involved in morphogenesis, cardiocyte differentiation, myosin filament organization, muscle organ morphogenesis, actomyosin structure organization, muscle system process		
Pcp4l1	Purkinje cell protein 4-like 1			
Myl6b	myosin, light polypeptide 6B	muscle contraction, striated muscle tissue development, actin filament-based movement, muscle organ development, actin-mediated cell contraction, muscle system process		

Lmod2	leiomodin 2	muscle contraction, actomyosin structure organization, cellular component assembly involved in morphogenesis, muscle cell differentiation, muscle system process		
Hspb7	heat shock protein family, member 7	actin cytoskeleton		
Smtnl1	smoothelin-like 1	response to activity, muscle organ morphogenesis, circulatory system process, regulation of blood circulation		
Myoz2	myozenin 2	muscle system process, striated muscle tissue development, actomyosin structure organization, second-messenger mediated signaling, inositol phosphate-mediated signaling, muscle cell differentiation, cellular component assembly involved in morphogenesis, muscle adaptation		
Myl2	myosin, light polypeptide 2	muscle system process, striated muscle tissue development, muscle organ morphogenesis, cardiac chamber development, regulation of the force of heart contraction, striated muscle contraction		
Atp2a2	ATPase, Ca^{2+} transporting, cardiac muscle, slow twitch 2	action potential, muscle system process, muscle cell differentiation, sarcoplasmic reticulum calcium ion transport, regulation of actin filament-based process, second-messenger-mediated signaling, regulation of neurotransmitter secretion, calcium-mediated signaling, relaxation of muscle, heart contraction, regulation of actin filament-based movement		
Tnni1	troponin I, skeletal, slow 1	muscle system process, muscle tissue development, muscle organ morphogenesis, cardiac chamber development, muscle adaptation		
Tecrl	trans-2,3-enoyl-CoA reductase-like	very long-chain fatty acid metabolic process, organic acid biosynthetic process, very long-chain fatty acid biosynthetic process, fatty acid metabolic process		
Tnnt1	troponin T1, skeletal, slow 1	actomyosin structure organization, musculoskeletal movement, cellular component assembly involved in morphogenesis,		

		multicellular organismal movement, muscle system process, muscle cell differentiation, muscle adaptation, heart contraction		
Sln	sarcolipin	muscle system process, regulation of ATPase activity, sarcoplasmic reticulum calcium ion transport, muscle relaxation		
Myh7b	myosin, heavy chain 7B, cardiac muscle	myofibril, myosin filament, actin cytoskeleton, myosin complex		
Homer 2	homer scaffolding protein 2	second-messenger-mediated signaling, inositol phosphate-mediated signaling, negative regulation of calcineurin-NFAT signaling cascade		
Xpo4	exportin 4	nuclear transport, positive regulation of establishment of protein localization, nuclear export. mRNA surveillance		

Table S2. Summarized gene ontologies present in genes of each cluster.

Cluster	Description	GO Term	Adjusted p-value
I	muscle system process	GO:0003012	1.30E-20
	skeletal muscle adaptation	GO:0043501	1.32E-14
	striated muscle adaptation	GO:0014888	3.41E-12
	muscle organ development	GO:0007517	2.53E-10
	muscle adaptation	GO:0043500	1.42E-09
	striated muscle tissue development	GO:0014706	1.14E-08
	muscle tissue development	GO:0060537	1.48E-08
	myofibril assembly	GO:0030239	1.41E-07
	muscle cell development	GO:0055001	7.38E-07
	cellular component assembly involved in morphogenesis	GO:0010927	1.28E-06
	muscle cell differentiation	GO:0042692	1.32E-06
	sarcomere organization	GO:0045214	1.69E-06
	negative regulation of calcineurin-NFAT signaling cascade	GO:0070885	4.91E-06
	striated muscle cell differentiation	GO:0051146	5.92E-06
	striated muscle cell development	GO:0055002	1.12E-05
	actomyosin structure organization	GO:0031032	1.62E-05
	negative regulation of calcium-mediated signaling	GO:0050849	2.20E-05
	regulation of calcineurin-NFAT signaling cascade	GO:0070884	6.60E-05
	calcineurin-NFAT signaling cascade	GO:0033173	1.18E-04
	calcineurin-mediated signaling	GO:0097720	1.46E-04
	inositol phosphate-mediated signaling	GO:0048016	1.88E-04
	skeletal muscle tissue development	GO:0007519	2.87E-04
	skeletal muscle organ development	GO:0060538	3.42E-04
	calcium-mediated signaling	GO:0019722	3.90E-04
	regulation of calcium-mediated signaling	GO:0050848	9.14E-04
	second-messenger-mediated signaling	GO:0019932	5.45E-03
I I	actomyosin structure organization	GO:0031032	1.62E-05
	cardiac muscle tissue development	GO:0048738	4.35E-05
	heart morphogenesis	GO:0003007	5.88E-05
	response to activity	GO:0014823	3.57E-03
	myofibril	GO:0030016	1.36E-20
	contractile fiber	GO:0043292	1.69E-20
	actin cytoskeleton	GO:0015629	1.89E-19
	sarcomere	GO:0030017	1.09E-15
	myosin complex	GO:0016459	4.58E-10
	myosin filament	GO:0032982	4.23E-08
	I band	GO:0031674	1.02E-07
	striated muscle thin filament	GO:0005865	1.18E-07
	myofilament	GO:0036379	2.06E-07
	A band	GO:0031672	7.75E-07
	M band	GO:0031430	9.48E-06
	Z disc	GO:0030018	2.43E-03
	actin binding	GO:0003779	8.08E-16
	actin filament binding	GO:0051015	5.18E-06
	motor activity	GO:0003774	8.70E-06
	calmodulin binding	GO:0005516	1.32E-02

III	muscle system process	GO:0003012	1.30E-20
	muscle contraction	GO:0006936	7.17E-17
	skeletal muscle adaptation	GO:0043501	1.32E-14
	striated muscle adaptation	GO:0014888	3.41E-12
	transition between fast and slow fiber	GO:0014883	1.30E-11
	regulation of skeletal muscle adaptation	GO:0014733	1.87E-10
	muscle organ development	GO:0007517	2.53E-10
	muscle adaptation	GO:0043500	1.42E-09
	striated muscle contraction	GO:0006941	8.73E-09
	striated muscle tissue development	GO:0014706	1.14E-08
	muscle organ morphogenesis	GO:0048644	1.21E-08
	muscle tissue development	GO:0060537	1.48E-08
	ventricular cardiac muscle tissue morphogenesis	GO:0055010	5.54E-08
	cardiac muscle contraction	GO:0060048	7.20E-08
	regulation of muscle system process	GO:0090257	8.75E-08
	ventricular cardiac muscle tissue development	GO:0003229	1.01E-07
	cardiac muscle tissue morphogenesis	GO:0055008	1.67E-07
	regulation of muscle contraction	GO:0006937	1.83E-07
	cardiac ventricle morphogenesis	GO:0003208	2.60E-07
	muscle tissue morphogenesis	GO:0060415	3.40E-07
	regulation of the force of heart contraction	GO:0002026	4.24E-07
	regulation of muscle adaptation	GO:0043502	7.38E-07
	skeletal muscle contraction	GO:0003009	1.06E-06
	heart contraction	GO:0060047	1.06E-06
	heart process	GO:0003015	1.28E-06
	muscle filament sliding	GO:0030049	1.34E-06
	actin-myosin filament sliding	GO:0033275	2.29E-06
	multicellular organismal movement	GO:0050879	3.39E-06
	musculoskeletal movement	GO:0050881	3.39E-06
	cardiac chamber morphogenesis	GO:0003206	3.49E-06
	cardiac ventricle development	GO:0003231	3.49E-06
	cardiac chamber development	GO:0003205	1.21E-05
	actin-mediated cell contraction	GO:0070252	2.02E-05
	regulation of blood circulation	GO:1903522	3.67E-05
	cardiac muscle tissue development	GO:0048738	4.35E-05
	actin filament-based movement	GO:0030048	5.88E-05
	heart morphogenesis	GO:0003007	5.88E-05
	regulation of heart contraction	GO:0008016	2.24E-04
	regulation of striated muscle contraction	GO:0006942	5.22E-04
	muscle hypertrophy in response to stress	GO:0003299	1.87E-03
	cardiac muscle hypertrophy in response to stress	GO:0014898	1.87E-03
	cardiac muscle adaptation	GO:0014887	1.98E-03
	regulation of actin filament-based movement	GO:1903115	5.82E-03
	regulation of actin filament-based process	GO:0032970	4.00E-02
IV	muscle system process	GO:0003012	1.30E-20
	muscle contraction	GO:0006936	7.17E-17
	skeletal muscle adaptation	GO:0043501	1.32E-14
	striated muscle adaptation	GO:0014888	3.41E-12
	transition between fast and slow fiber	GO:0014883	1.30E-11

	regulation of skeletal muscle adaptation	GO:0014733	1.87E-10
	muscle organ development	GO:0007517	2.53E-10
	muscle adaptation	GO:0043500	1.42E-09
	striated muscle contraction	GO:0006941	8.73E-09
	striated muscle tissue development	GO:0014706	1.14E-08
	muscle organ morphogenesis	GO:0048644	1.21E-08
	muscle tissue development	GO:0060537	1.48E-08
	ventricular cardiac muscle tissue morphogenesis	GO:0055010	5.54E-08
	cardiac muscle contraction	GO:0060048	7.20E-08
	regulation of muscle system process	GO:0090257	8.75E-08
	ventricular cardiac muscle tissue development	GO:0003229	1.01E-07
	myofibril assembly	GO:0030239	1.41E-07
	cardiac muscle tissue morphogenesis	GO:0055008	1.67E-07
	regulation of muscle contraction	GO:0006937	1.83E-07
	cardiac ventricle morphogenesis	GO:0003208	2.60E-07
	muscle tissue morphogenesis	GO:0060415	3.40E-07
	regulation of the force of heart contraction	GO:0002026	4.24E-07
	regulation of muscle adaptation	GO:0043502	7.38E-07
	muscle cell development	GO:0055001	7.38E-07
	skeletal muscle contraction	GO:0003009	1.06E-06
	heart contraction	GO:0060047	1.06E-06
	cellular component assembly involved in morphogenesis	GO:0010927	1.28E-06
	heart process	GO:0003015	1.28E-06
	muscle cell differentiation	GO:0042692	1.32E-06
	muscle filament sliding	GO:0030049	1.34E-06
	sarcomere organization	GO:0045214	1.69E-06
	actin-myosin filament sliding	GO:0033275	2.29E-06
	multicellular organismal movement	GO:0050879	3.39E-06
	musculoskeletal movement	GO:0050881	3.39E-06
	cardiac chamber morphogenesis	GO:0003206	3.49E-06
	cardiac ventricle development	GO:0003231	3.49E-06
	negative regulation of calcineurin-NFAT signaling cascade	GO:0070885	4.91E-06
	striated muscle cell differentiation	GO:0051146	5.92E-06
	striated muscle cell development	GO:0055002	1.12E-05
	cardiac chamber development	GO:0003205	1.21E-05
	actomyosin structure organization	GO:0031032	1.62E-05
	actin-mediated cell contraction	GO:0070252	2.02E-05
	negative regulation of calcium-mediated signaling	GO:0050849	2.20E-05
	regulation of blood circulation	GO:1903522	3.67E-05
	cardiac muscle tissue development	GO:0048738	4.35E-05
	actin filament-based movement	GO:0030048	5.88E-05
	heart morphogenesis	GO:0003007	5.88E-05
	regulation of calcineurin-NFAT signaling cascade	GO:0070884	6.60E-05
	calcineurin-NFAT signaling cascade	GO:0033173	1.18E-04
	calcineurin-mediated signaling	GO:0097720	1.46E-04
	inositol phosphate-mediated signaling	GO:0048016	1.88E-04
	regulation of heart contraction	GO:0008016	2.24E-04
	skeletal muscle tissue development	GO:0007519	2.87E-04
	skeletal muscle organ development	GO:0060538	3.42E-04
	calcium-mediated signaling	GO:0019722	3.90E-04
	regulation of striated muscle contraction	GO:0006942	5.22E-04

	regulation of calcium-mediated signaling	GO:0050848	9.14E-04
	muscle hypertrophy in response to stress	GO:0003299	1.87E-03
	cardiac muscle hypertrophy in response to stress	GO:0014898	1.87E-03
	cardiac muscle adaptation	GO:0014887	1.98E-03
	sarcoplasmic reticulum calcium ion transport	GO:0070296	2.26E-03
	relaxation of muscle	GO:0090075	2.71E-03
	response to activity	GO:0014823	3.57E-03
	second-messenger-mediated signaling	GO:0019932	5.45E-03
	regulation of actin filament-based movement	GO:1903115	5.82E-03
	regulation of actin filament-based process	GO:0032970	4.00E-02
	calcium ion transport	GO:0006816	4.14E-02